Cell Reports

Article

Autism-associated CHD8 controls reactive gliosis and neuroinflammation via remodeling chromatin in astrocytes

Graphical abstract

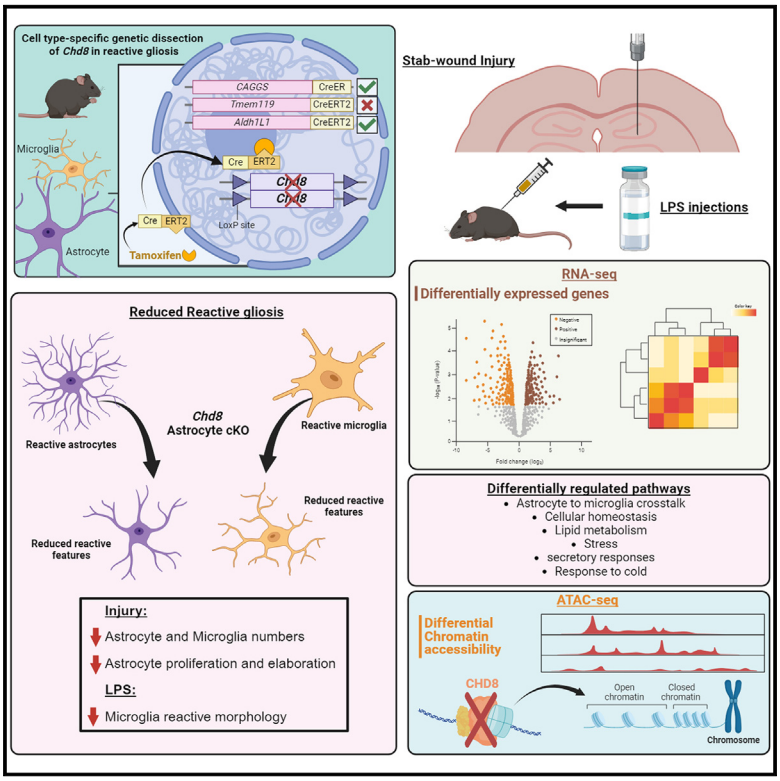

Highlights

- Astrocytic CHD8 in the adult brain regulates injury-induced reactive gliosis
- Astrocytic CHD8 in the adult brain controls LPS-induced neuroinflammation
- Astrocytic CHD8 regulates chromatin accessibility and transcription during neuroinflammation
- AAV- and CRISPR-mediated direct *Chd8* editing in astrocytes *in vivo* attenuates reactive gliosis

Authors

Platon Megagiannis, Yuan Mei, Rachel E. Yan, ..., Trey Ideker, Neville E. Sanjana, Yang Zhou

Correspondence

tideker@ucsd.edu (T.I.), yang.zhou7@mcgill.ca (Y.Z.)

In brief

Megagiannis et al. revealed the role of autism-associated CHD8 in reactive gliosis and neuroinflammation through regulating chromatin landscape and gene transcription in astrocytes.

Megagiannis et al., 2024, Cell Reports *43*, 114637
August 27, 2024
https://doi.org/10.1016/j.celrep.2024.114637

CellPress

Cell Reports

CellPress
OPEN ACCESS

Article

Autism-associated CHD8 controls reactive gliosis and neuroinflammation via remodeling chromatin in astrocytes

Platon Megagiannis,[1,11] Yuan Mei,[2,3,11] Rachel E. Yan,[4,5] Lin Yuan,[1] Jonathan J. Wilde,[6,7] Hailey Eckersberg,[1] Rahul Suresh,[1] Xinzhu Tan,[1] Hong Chen,[1] W. Todd Farmer,[8] Kuwook Cha,[9] Phuong Uyen Le,[1] Helene Catoire,[1] Daniel Rochefort,[1] Tony Kwan,[10] Brian A. Yee,[3] Patrick Dion,[1] Arjun Krishnaswamy,[9] Jean-Francois Cloutier,[1] Stefano Stifani,[1] Kevin Petrecca,[1] Gene W. Yeo,[3] Keith K. Murai,[8] Guoping Feng,[6,7] Guy A. Rouleau,[1] Trey Ideker,[2,*] Neville E. Sanjana,[4,5] and Yang Zhou[1,12,*]

[1]Department of Neurology and Neurosurgery, Montreal Neurological Institute-Hospital, Faculty of Medicine and Health Sciences, McGill University, Montreal, QC, Canada
[2]Division of Genetics, Department of Medicine, University of California, San Diego, San Diego, CA, USA
[3]Department of Cellular and Molecular Medicine, Stem Cell Program, Institute for Genomic Medicine, University of California, San Diego, La Jolla, CA, USA
[4]New York Genome Center, New York, NY, USA
[5]Department of Biology, New York University, New York, NY, USA
[6]Department of Brain and Cognitive Sciences, McGovern Institute for Brain Research, Massachusetts Institute of Technology (MIT), Cambridge, MA, USA
[7]Stanley Center for Psychiatric Research, Broad Institute of MIT and Harvard, Cambridge, MA, USA
[8]Centre for Research in Neuroscience, Department of Neurology and Neurosurgery, Brain Repair and Integrative Neuroscience Program, The Research Institute of the McGill University Health Center, Montreal General Hospital, Montreal, QC, Canada
[9]Department of Physiology, Faculty of Medicine and Health Sciences, McGill University, Montreal, QC, Canada
[10]McGill Genome Center and Department of Human Genetics, McGill University, Montreal, QC, Canada
[11]These authors contributed equally
[12]Lead contact
*Correspondence: tideker@ucsd.edu (T.I.), yang.zhou7@mcgill.ca (Y.Z.)
https://doi.org/10.1016/j.celrep.2024.114637

SUMMARY

Reactive changes of glial cells during neuroinflammation impact brain disorders and disease progression. Elucidating the mechanisms that control reactive gliosis may help us to understand brain pathophysiology and improve outcomes. Here, we report that adult ablation of autism spectrum disorder (ASD)-associated CHD8 in astrocytes attenuates reactive gliosis via remodeling chromatin accessibility, changing gene expression. Conditional *Chd8* deletion in astrocytes, but not microglia, suppresses reactive gliosis by impeding astrocyte proliferation and morphological elaboration. Astrocyte *Chd8* ablation alleviates lipopolysaccharide-induced neuroinflammation and septic-associated hypothermia in mice. Astrocytic CHD8 plays an important role in neuroinflammation by altering the chromatin landscape, regulating metabolic and lipid-associated pathways, and astrocyte-microglia crosstalk. Moreover, we show that reactive gliosis can be directly mitigated *in vivo* using an adeno-associated virus (AAV)-mediated *Chd8* gene editing strategy. These findings uncover a role of ASD-associated CHD8 in the adult brain, which may warrant future exploration of targeting chromatin remodelers in reactive gliosis and neuroinflammation in injury and neurological diseases.

INTRODUCTION

Neuroinflammation in the CNS constitutes cascades of pathophysiological processes to signal altered brain homeostasis. Reactive gliosis is a hallmark of damage and inflammatory processes resulting from injury, infection, and diseases. Reactive gliosis can be induced by acute, focal damage that leads to tissue reorganization and repair, or chronic and diffuse insults that lead to homeostatic and physiological changes in neurons and glia.[1,2] Although the neurotoxic and neuroprotective outcomes of reactive gliosis and their functional impact remain poorly understood, exaggerated reactive gliosis may cause excessive inflammation and induce neuronal death and tissue damage.[3] Upon mechanical and inflammatory insults, glial cells undergo profound remodeling at the molecular, cellular, and functional levels, with progressive changes in gene transcription, morphology, and proliferation.[1,4–9] Recent studies using mouse and human induced pluripotent stem cell (iPSC)-derived astrocytes revealed diverse changes in chromatin accessibility through substantial chromatin remodeling during astrocyte

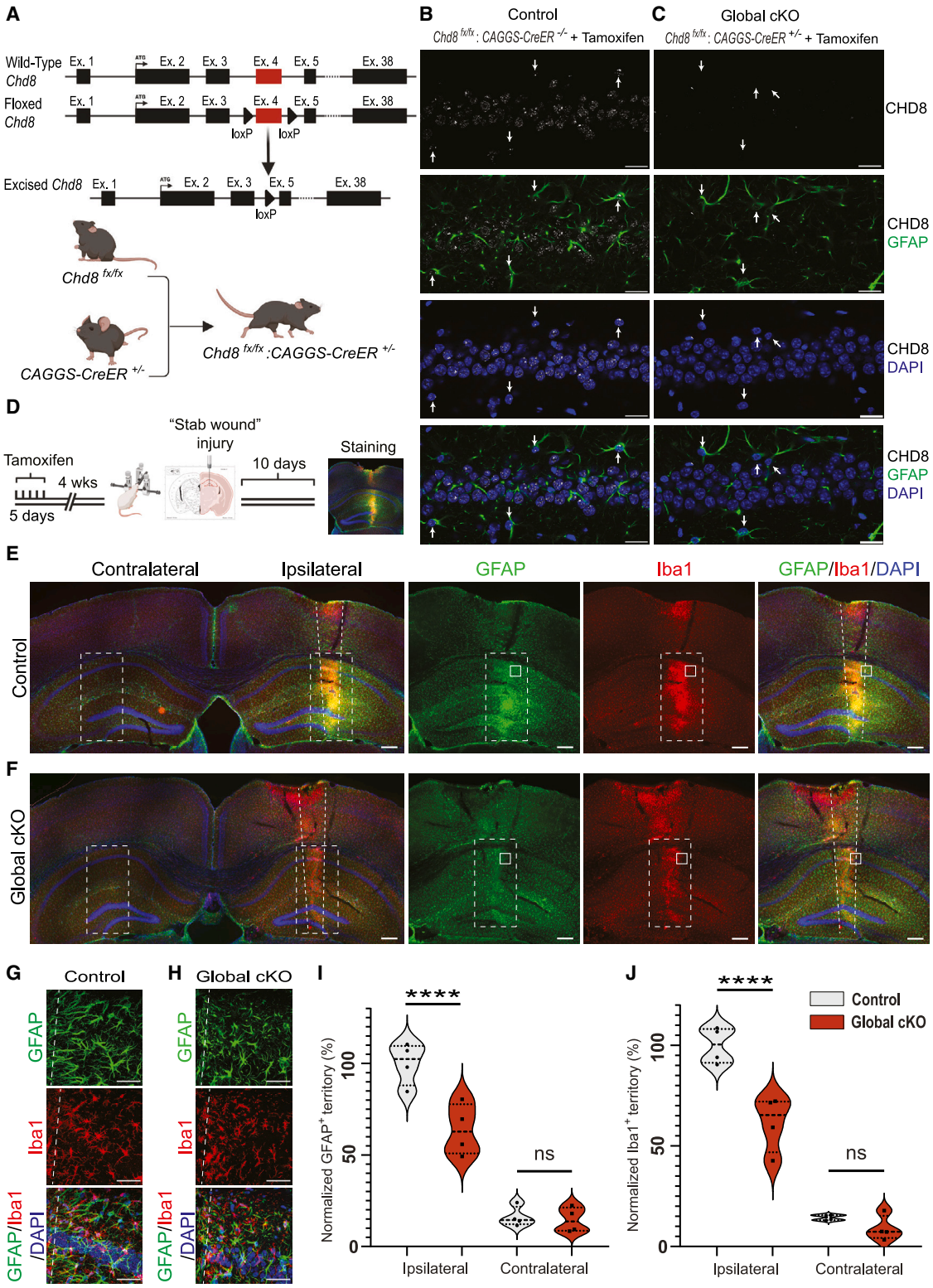

Figure 1. Reduced reactive gliosis in the global *Chd8*-cKO mice in the stab-wound injury model

(A) Genetic strategy targeting exon 4 of the *Chd8* gene. The exon was flanked with *loxP* sites to excise the loci, resulting in a frameshift mutation that disrupts the production of the CHD8 protein after Cre excision.

(legend continued on next page)

reactivity.[10–12] Despite this progress, the chromatin remodelers and epigenetic pathways that orchestrate gliosis in the brain remain largely unknown. Precise dissection of chromatin remodeling factors that allow for beneficially modulating reactive gliosis may offer therapeutic strategies for neurological and neurodegenerative disorders.[10,13,14]

Chromatin remodeling factors are proteins that modify chromatin dynamics in the genome by forming protein complexes that modulate the accessibility of DNA and calibrate gene transcription.[15] Chromodomain helicase DNA-binding protein 8 (CHD8) encodes a member of the CHD family of proteins, which is a high-confidence genetic risk factor for autism spectrum disorder (ASD) and neurodevelopmental disorders, and relevant to cancers.[16–18] As a member of the SNF2H-like, ATP-dependent subfamily of chromatin remodelers, CHD8 acts by regulating nucleosome spacing and histone H3.3 incorporation.[19–22] CHD8 controls multiple transcriptional pathways, including Wnt signaling and p53-dependent transactivation.[23] CHD8 cooperates with SOX (Sry-related HMG box) and other transcriptional factors to coordinate pluripotency and differentiation in neural stem cells.[24] Previous studies of *Chd8* in the nervous system using model organisms concentrated on the functional aspects of CHD8 in stem cells and the developing brain, which provide enormous insight into the neurobiology of ASD.[25–31] However, little is known about CHD8 and its function in physiology and disease in the adult brain.

When characterizing *Chd8* mutant animals, we observed altered glial scar formation after stereotaxic intracranial injections. This preliminary observation led us to hypothesize that pathogenic stimuli and neuroinflammation elicit chromatin remodeling via CHD8 in glia, resulting in specialized transcriptional programs to promote glial reactivity. We engineered a floxed *Chd8* strain that allows for tamoxifen-inducible ablation of *Chd8* from adult mice. In a stab-wound model of brain injury, we demonstrate that *Chd8* ablation in astrocytes, but not microglia, alleviates reactive gliosis. Mechanistically, we found CHD8 to be essential for astrocyte proliferation, process elaboration, and cellular hypertrophy upon acute injury. Utilizing a lipopolysaccharide (LPS)-induced neuroinflammatory paradigm, we found that CHD8-mediated transcriptional programs in astroglia play critical roles in mediating crosstalk between astrocyte and microglia and promoting neuroinflammation. We identified and validated pathways related to cellular metabolism and lipid biosynthesis resulting from *Chd8* conditional knockout (cKO) in astrocytes during LPS-induced neuroinflammation. We show that CHD8 shapes the landscape of chromatin accessibility during LPS-induced neuroinflammation. Furthermore, we demonstrated the translational potential for mitigating injury-induced reactive gliosis through astrocyte-specific *Chd8* ablation *in vivo*, utilizing an adeno-associated virus (AAV)-mediated delivery of CRISPR-SaCas9 (*Staphylococcus aureus* Cas9) to the mouse brain. In summary, this study reveals an important role of CHD8-mediated chromatin remodeling in astrocytes during injury and LPS-induced neuroinflammation. Our results highlight CHD8 in astrocytes as a potential therapeutic target against pathogenic gliosis associated with the neuroinflammatory process in brain injuries and diseases.

RESULTS

Global *Chd8* ablation in adult mouse brain diminishes injury-induced reactive gliosis

We previously showed that disruption of exon 4 of the *Chd8* gene is sufficient to globally knock out *Chd8* and cause embryonic lethality in homozygotic mutant mice.[32] To bypass the lethality and enable conditional *Chd8* ablation in adult mice for functional characterization, we engineered a mouse strain by flanking exon 4 of *Chd8* with *loxP* sites through CRISPR-Cas9-mediated gene editing in zygotes (Figures 1A and S1A). We bred the *Chd8*$^{fx/fx}$ mice with the *CAGGS-CreER* line (Figure 1A), which features a global and widespread expression of CreER in the brain and peripheral tissues that is activated upon the administration of tamoxifen.[33,34] Three weeks post-administration of tamoxifen into adult mice, CHD8 was undetectable in neurons and astrocytes as revealed by immunohistochemistry with CHD8 antibodies in the global cKO group (Figures 1B and 1C). To test our hypothesis and delineate the role of CHD8 in reactive gliosis, we first chose to adopt the stab-wound injury model. An experimental model that mimics acute and focal damage resulting from traumatic brain injury in humans.[35–37] Previous studies of the stab-wound model have characterized that 10 days post-injury (dpi) allows for observing the maximum response from both microglia and astrocytes.[38,39] Mice in both global *Chd8*-cKO and age-matched control groups were injured with the same parameters, and brain slices were examined at 10 dpi through immunohistochemistry (Figure 1D).

To characterize reactive gliosis, we prepared serial brain slices encompassing the injury site, and stained with GFAP and Iba1,

(B and C) Representative images of CHD8 in the CA1 regions of adult mouse brains. CHD8 is expressed in neurons and astrocytes in controls (B). After tamoxifen administration, *Chd8*$^{fx/fx}$*: CAGGS-CreER*$^{+/-}$ mouse brains showed non-detectable levels of CHD8 protein (C). In both (B) and (C), arrows point to astrocytes expressing CHD8 and its knockout thereafter.

(D) Schematic diagram for tamoxifen-induced *Chd8* cKO, the stab-wound injury model, and the analysis of reactive gliosis.

(E and F) Response of GFAP$^+$ astrocytes and Iba1$^+$ microglia after stab-wound injury. Control mice (E) exhibit astrocytic and microglial response as expected, while global *Chd8* cKO mice (F) show reduced staining for both GFAP$^+$ and Iba1$^+$ along the needle track.

(G and H) High-magnification images from the injury site from the corresponding genotypes. Note the reduction in cell body size, process elongation, and polarity in astrocytes from global *Chd8* cKO mice (H).

(I and J) Decreased area occupied by GFAP$^+$ astrocytes (I) and Iba1$^+$ microglia (J) in global *Chd8* cKO mice compared to controls.

In (B) and (C), scale bars indicate 20 μm; in (G) and (H), scale bars indicate 50 μm; in (E) and (F), scale bars indicate 500 μm. The dashed rectangle indicates the ROIs that were quantified. In (E)–(H), the dashed lines indicate the needle track of the injury. In (I) and (J), data points illustrate the quantified area from the six brain slices most proximal to the injury epicenter. Data are normalized to the means of the ipsilateral site in control mice. ****$p < 0.0001$, ns, not significant; statistical analysis was performed with two-way ANOVA; on the violin plots, dashed lines indicate the 25%, mean, and 75% percentile, respectively, from bottom to top; n = 4 mice per genotype.

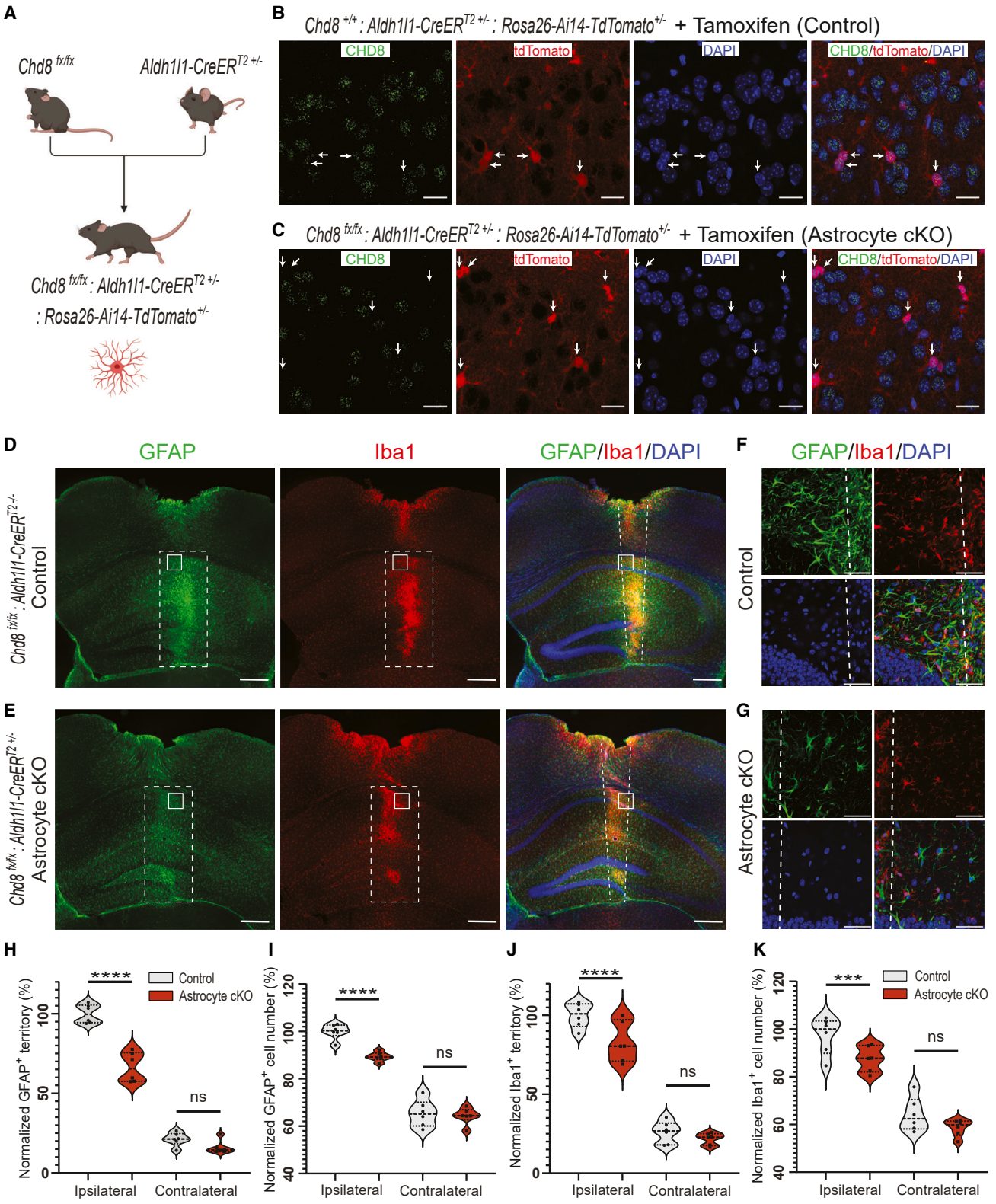

Figure 2. Reduced reactive gliosis in astrocyte *Chd8*-cKO mice in the stab-wound injury model

(A) Strategy for tamoxifen-induced, astrocyte-specific *Chd8* cKO utilizing the *Aldh1l1-CreERT2* line. Mice were crossed with the Ai14-*tdTomato* reporter line to visualize recombined cells.

(legend continued on next page)

two classical markers for reactive astrocytes and microglia, respectively[10,40] (Figures S2A and S2B). The stab-wound injury resulted in a robust increase in both GFAP and Iba1 signals in the ipsilateral as compared to the contralateral (uninjured) side (Figures 1E, 1F, 1I, and 1J). The signal threshold for quantification was determined by the Moments algorithm in ImageJ, using the contralateral side of each slice as a reference (Figures 1E and 1F). We applied the thresholding value to calculate the signal area for the region of interest (ROI) set at the hippocampal region on the ipsilateral side and quantified the area occupied by the GFAP and Iba1 signals around the injury site (Figures 1E, 1F, and S3A–S3E), as described previously.[41] This analytic pipeline was applied to all serial sections, and comparisons were made between control and global cKO groups (Figures S4A–S4F). We found that the six slices most proximal to the epicenter of injury showed the most robust glial response (Figures S4A, S4B, S4E, and S4F). As compared to the control group (Figure 1E), the global *Chd8*-cKO group (Figure 1F) displayed significantly reduced GFAP and Iba1 signals at the site of the injury (Figures 1I and 1J). Higher-magnification images of the injury site revealed the typical response of GFAP$^+$ astrocytes and Iba1$^+$ microglia in the control group to a stab wound, with cell hypertrophy, polarization, and process elongation toward the needle track (Figure 1G). In contrast, both astrocytes and microglia in the global cKO group showed diminished morphological responses to injury (Figure 1H). The global *Chd8*-cKO group showed a 33.6% decrease in GFAP territory (Figure 1I) and a 38.57% decrease in Iba1 (Figure 1J) occupied territory. These data revealed a significant role of CHD8 in controlling glial response and promoting reactive gliosis upon injury in adult mouse brains.

Astrocytic but not microglial expression of *Chd8* in the adult brain is essential for injury-induced reactive gliosis

Given that *GAGGS-CreER* is expressed in all cell types, including neurons and glia, we next employed a set of CreER-expressing mouse strains to parse the cell types that CHD8 is acting through in reactive gliosis. In the CNS, astrocytes are one of the major mediators of neuroinflammation and the prime contributor to glial scar formation.[1,7,42] We examined the expression of CHD8 in astrocytes and the efficient deletion of *Chd8* using primary astrocyte cultures derived from *Chd8$^{fx/fx}$* mice (Figures S1B and S1C). We crossed the *Chd8$^{fx/fx}$* mouse with the *Aldh1l1-CreER^{T2}* line to specifically target astrocytes in the adult mouse brain (Figure 2A). The *Aldh1l1-CreER^{T2}* line is a highly specific, well-characterized strain that allows for selective recombination in astrocytes with minimal recombination in neurons in the adult cortex, striatum, and hippocampus.[43–47] We introduced the Ai14-*Rosa-tdTomato* transgene to visualize the *Aldh1l1-CreER^{T2}*-expressing astrocytes in both control and astrocyte-cKO groups *in vivo* (Figures 2A–2C). As shown in representative images taken from the cortex, we detected CHD8 protein in the nucleus from tdTomato$^+$ astrocytes in the control group (Figure 2B) but not from tdTomato$^+$ astrocytes in the astrocyte-cKO group (Figure 2C). These results confirm the efficient genetic ablation of CHD8 in the adult brain in astrocyte-cKO mice.

We returned to the stab-wound injury model and quantified the reactive gliosis *in vivo* in the control and astrocyte-cKO groups using the same experimental and analytic procedures as described for global cKO (Figure 1D). We quantified an identical ROI in the hippocampal region occupied by the GFAP and Iba1 signals around the injury site for all serial slices, as shown by images from a representative pair of mice in Figures S5A and S5B. As compared to the control group (Figure 2D), the astrocyte *Chd8*-cKO group (Figure 2E) showed significantly reduced GFAP and Iba1 signals at the site of injury (Figures 2H and 2J). High-magnification images from the injury site showed the typical response of GFAP$^+$ astrocytes and Iba1$^+$ microglia in the control group (Figure 2F), while astrocytes and microglia in the astrocyte cKO group show reduced cellular responses to injury (Figure 2G). Quantifying these differences, the astrocyte-cKO group showed a 33.6% decrease in GFAP$^+$ territory (Figure 2H). Remarkably, the Iba1$^+$ territory was also decreased compared to controls in these mice by 17.03% (Figure 2J). To further quantify the number of cells involved in reactive gliosis, we adopted an automated cell-counting algorithm, Cellpose, that was previously described.[48,49] The number of GFAP$^+$ and Iba1$^+$ cells decreased by 10.61% (Figure 2I) and 10.04% (Figure 2K), respectively. The comparison of all the slices for both territory and cell number metrics between the control and astrocyte-cKO groups (Figure S6) shows consistent changes as Figures 2H–2K. To exclude confounding factors resulting from the possible contribution of *Aldh1l1-CreER^{T2}* transgenes on gliosis, we compared mice from the control group (*Chd8$^{fx/fx}$*: *Aldh1l1-CreER$^{T2-/-}$*) with mice from a *CreER* transgenic group (*Chd8$^{+/+}$*: *Aldh1l1-CreER$^{T2+/-}$*) and found no difference between groups (Figure S7). Results from these control experiments indicate that the *Aldh1l1-CreER^{T2}* transgene and Cre activity do not

(B and C) Astrocyte-specific *Chd8*-cKO mice show non-detectable CHD8 protein expression in cortical slices. Controls are mice without the *Chd8* floxed alleles but expressing *Aldh1l1-CreERT2* to turn on the expression of tdTomato reporter. Arrows indicate CHD8 expression in tdTomato$^+$ astrocytes in control but not astrocyte *Chd8* cKO.

(D and E) GFAP and Iba1 staining of astrocytes and microglia, respectively, after stab-wound injury in control (D) and astrocyte cKO mice (E).

(F and G) High-magnification images from the injury sites from the corresponding genotypes showing reduction in cell body size, process elongation, and polarity in astrocytes and reduced microglia numbers in astrocyte cKO mice.

(H and I) Decreased area occupied by GFAP$^+$ astrocytes and their numbers in astrocyte cKO mice compared to controls.

(J and K) Decreased area occupied by Iba1$^+$ microglia and their numbers in astrocyte cKO mice compared to controls.

In (H)–(K), data points represent the quantified area from the six brain slices most proximal to the injury epicenter. Data are normalized to the means of the ipsilateral site in control mice. In (B) and (C), scale bars indicate 20 μm; in (F) and (G), scale bars indicate 50 μm; in (D) and (E), scale bars indicate 500 μm. The dashed rectangle indicates the ROIs that were quantified. In (D)–(G), the dashed lines in merged images indicate the needle track of the injury. In (H)–(K), ***$p < 0.001$; ****$p < 0.0001$; ns, not significant; statistical comparisons were analyzed with two-way ANOVA; on the violin plots, dashed lines indicate the 25%, mean, and 75% percentile, respectively, from bottom to top; $n = 6$ mice per genotype.

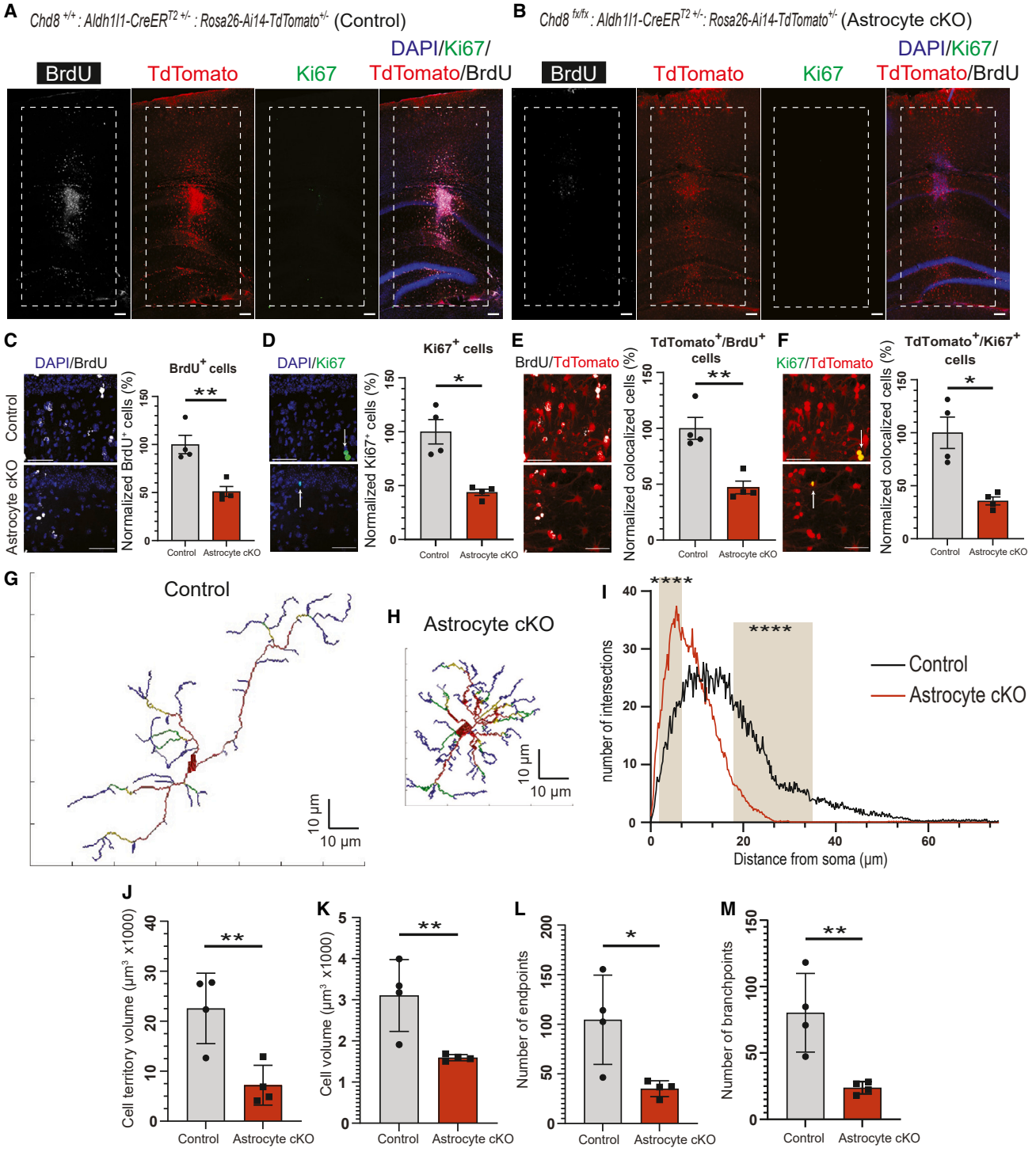

Figure 3. Reduced proliferation and impaired morphological changes of reactive astrocytes in astrocyte *Chd8*-cKO mice

(A and B) Representative images show reduced staining for proliferation markers (BrdU and Ki67) after stab-wound injury in astrocyte cKO mice (B) as compared to control mice (A). The dashed rectangle indicates the ROI used to quantify $BrdU^+$ and $Ki67^+$ cells in (C)–(F).

(C) Decreased $BrdU^+$ nuclei in the astrocyte cKO mice as shown by high-magnification images and quantification.

(D) Reduced $Ki67^+$ nuclei in the astrocyte cKO mice.

(E) Decreased proliferation of $tdTomato^+$ astrocytes from astrocyte cKO mice as shown by reduced $tdTomato^+/BrdU^+$ colocalized cells.

(F) Decreased proliferation of $tdTomato^+$ astrocytes from astrocyte cKO mice as shown by reduced $tdTomato^+/BrdU^+$ colocalized cells.

(G and H) Representative skeletonized images of two astrocytes from control (G) and astrocyte cKO mice (H).

(legend continued on next page)

contribute to the observed reduction of injury-induced reactive gliosis.

We also sought to interrogate the role of CHD8 in microglia in the context of injury-induced gliosis, as microglia play an integral role in the initiation as well as the maintenance of the inflammatory response.[1,50] We crossed *Chd8*$^{fx/fx}$ mice harboring Ai14-*Rosa-tdTomato* with a *Tmem119-CreER*^{T2} mouse line, a highly specific and well-characterized CreER^{T2} line for microglia.[40,51–53] Interestingly, we did not detect CHD8 protein in the nucleus from the tdTomato^{+} microglia in either control (Figure S8A) or microglia cKO groups (Figure S8B). We reason that the limitation of immunohistochemistry and the sensitivity of antibodies may prevent the detection of low levels of CHD8 protein expression in the microglial cells. Therefore, we proceeded with the same stab-wound injury paradigm as described above. We did not find a difference regarding signal territory and cell numbers between groups (Figures S8C–S8H and S9). These data suggest that *Chd8* in microglia is dispensable for stab-wound injury-induced reactive gliosis. Taken together, these results indicate that *Chd8* ablation in astrocytes but not microglia reduces injury-induced gliosis, recapitulating the attenuated response of astrocytes and microglia observed in the global cKO mice.

Reduced proliferation and elaboration of *Chd8*-ablated astrocytes after stab-wound injury

Upon mechanical injury, astrocytes react quickly by initiating local proliferation, preferably at juxtavascular locations, and by changing their morphology to become hypertrophic and elongated. They also extend long processes toward the injury site *in vivo*.[2,7,54] We thus carried out experiments to assay these features in astrocytes subjected to stab-wound injury. We injected bromodeoxyuridine (BrdU) into mice in both control and astrocyte cKO groups to label and quantify proliferating astrocytes and other dividing cells as previously described.[35] We found reduced proliferation in the astrocyte-cKO group (Figures 3B and 3C) as compared to controls (Figures 3A and 3C). We also counterstained the same set of slices with the proliferative marker Ki67 to detect cells that were actively dividing. Consistent with BrdU staining, we observed reduced Ki67^{+} cells in the astrocyte cKO group compared to controls (Figures 3A, 3B, and 3D). Upon stab-wound injury, multiple types of cells may undergo proliferation. The tdTomato-labeled astrocytes in both control and astrocyte cKO groups allow us to dissect further mechanisms (Figure 2A). Colocalization analysis of tdTomato^{+} astrocytes with both proliferation markers further revealed a significant reduction in the astrocyte cKO group. We found a 52.83% decrease in tdTomato^{+}/BrdU^{+} cells (Figure 3E) and a 64.31% decrease in tdTomato^{+}/Ki67^{+} cells (Figure 3F) in the astrocyte-cKO group as compared to controls. These data reveal that *Chd8*-ablated astrocytes undergo impaired dividing and proliferation upon stab-wound injury.

Next, we used tdTomato to trace and examine astrocyte morphology. We used 3DMorph MATLAB software to segment and quantify the morphology of astrocytes obtained within 300 μm from the injury site.[55,56] We performed Sholl analysis on the skeletonized images generated through the software and revealed differential astrocyte branch and morphological parameters between genotypes (Figures 3G and 3H). Specifically, reactive astrocytes in the astrocyte cKO group have larger numbers of processes proximal to the soma, while astrocytes from the control group display larger numbers of processes extending distally from the soma (Figure 3I). We then quantified characteristic morphological variables for astrocytes.[55,56] We found several parameters to be reduced, including occupied territory, cellular volume, number of endpoints, and number of branch points in the astrocyte cKO group (Figures 3J–3M). Taken together, these data reveal a crucial role of CHD8 in controlling the proliferation and morphological elaboration of reactive astrocytes upon stab-wound injury.

Astrocytic expression of *Chd8* in the adult brain is required for LPS-induced neuroinflammation

To further investigate the role of CHD8 in neuroinflammation, we utilized a widely used systematic and diffuse paradigm of neuroinflammation through the injection of LPS. We used a single dose of LPS in high concentration (5 mg/kg, intraperitoneal injection) to stimulate a temporary and reliable inflammatory reaction, as described previously.[57–60] We chose 3 days post-LPS injection to capture a robust response of microglial cells, which are recognized to be the major reactive cells in this model.[1,57,61,62] Consistent with previous reports on LPS models in mice,[57,63] we did not detect a significant change in GFAP^{+} cells in either LPS-treated control mice (Figure 4B) or LPS-treated astrocyte cKO mice (Figure 4C), when compared to saline-treated control mice (Figure 4A). In the same set of brain slices, we observed a robust increase in Iba1^{+} signal in LPS-treated control mice (Figure 4B), but only a mild increase in LPS-treated astrocyte cKO mice (Figure 4C) as compared to saline-treated control mice (Figure 4A). We observed attenuated enlargement of cell bodies and less pronounced ameboid shape formation in microglia from the astrocyte cKO mice compared to controls (Figures 4D and 4E). Sholl analysis of individual Iba1^{+} microglia using 3DMorph (Figures 4F and 4G) revealed reduced numbers of intersections in microglia from astrocyte cKO mice as compared to control mice (Figure 4H). Further characterization of microglial morphology

(I) Sholl analysis of astrocytes localized within 300 μm of the needle track revealed reduced intersections in astrocyte cKO mice at distances between 18 and 35 μm from the soma, indicating reduced cell elongation. Conversely, astrocyte cKO mice featured astrocytes with processes concentrated closer to the cell soma (n = 24 cells from 4 mice per genotype).

(J) Decreased territory volume of astrocytes from astrocyte cKO mice, indicating reduced hypertrophy and elongation toward the injury site.

(K) Smaller cellular volume in astrocytes from astrocyte cKO mice.

(L and M) Fewer endpoints (L) and reduced number of branchpoints (M) in astrocytes from astrocyte cKO mice.

In (A) and (B), scale bars indicate 200 μm; in (C)–(F), scale bars indicate 50 μm. The dashed rectangles indicate the areas that were quantified. *p < 0.05; **p < 0.01; ****p < 0.0001; ns, not significant. Statistical comparisons were analyzed with the two-tailed Welch's t test; error bars indicate the SEMs. In (I), asterisks indicate the range where the number of intersections is significantly different, analyzed through the mixed-effects model. In (C)–(F) and (J)–(M), n = 4 mice per genotype.

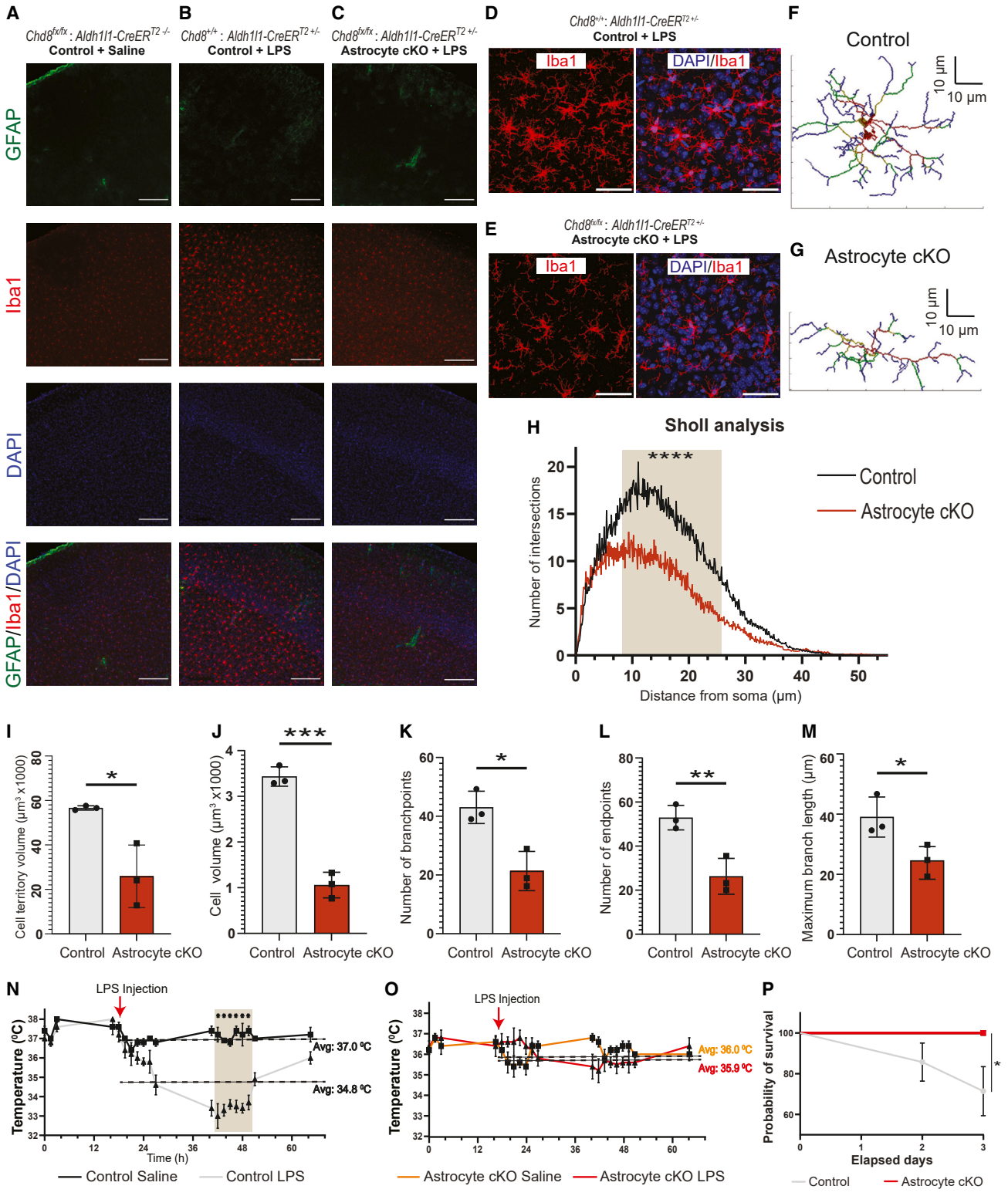

Figure 4. Impaired microglial response and alleviated hypothermia in LPS-treated astrocyte cKO mice

(A–C) Representative images from the cortex of saline-treated control mice (A), LPS-treated control mice (B), and LPS-treated astrocyte cKO mice (C). GFAP$^+$ staining does not show a difference between genotypes after LPS stimulation. In LPS-treated astrocyte cKO mice (C), microglia reactivity, as indicated by the Iba1$^+$ signal, is reduced as compared to controls (B).

(legend continued on next page)

revealed a consistent decrease in parameters, including cell territory volume (Figure 4I), cell volume (Figure 4J), branch points (Figure 4K), number of endpoints (Figure 4L), and maximum branch length (Figure 4M).

In both control and astrocyte cKO groups, we monitored body temperature, collected brains for immunohistochemistry, and extracted RNA for transcriptomic analysis, as illustrated in Figure S10A. In the control group, we observed a significant drop in body temperature (hypothermia) in mice receiving LPS compared to saline-injected mice (Figure 4N), consistent with well-documented effects of LPS on body temperature.[59,64] Interestingly, in astrocyte cKO groups, neither LPS- nor saline-treated mice exhibited a drop in body temperature (Figure 4O). Moreover, we observed a beneficial effect on LPS-induced systematic inflammation in the astrocyte cKO group, as reflected by alleviated sepsis-induced hypothermia. Four out of 14 (4/14) mice in the control group reached the humane endpoint of hypothermia (at 29°C body temperature) and had to be euthanized (Figure 4P). In contrast, all the mice (16/16) from the *Chd8* astrocyte cKO group maintained normal body temperature and survived during the same period (Figure 4P). We also performed a panel of behavioral tests after LPS treatment in both genotypes. However, we did not observe a significant difference between LPS-treated control and astrocyte cKO mice (Figure S11), possibly due to the small sample size. These results indicate that CHD8 in astrocytes is required for LPS-induced microglia reactivity and systemic inflammatory response, presumably through regulating astrocyte-derived signaling molecules and mediating the crosstalk between astrocytes and microglia.

Transcriptomic pathways related to lipid metabolism and cellular homeostasis are modulated by CHD8 in astrocytes following neuroinflammation

We asked whether ablation of *Chd8* in astrocytes may have altered their transcriptome and pre-conditioned the brain to atypical states prior to inflammatory insults. Using cortical tissue, we performed bulk RNA sequencing (RNA-seq) in astrocyte cKO and control mice without subjecting them to injury or LPS stimulation. The bioinformatics analysis from bulk RNA-seq, however, did not identify genes that were differentially expressed between astrocyte cKO and controls with a false discovery rate (FDR) of <0.1 (Figures S10B and S10C). These results suggest that *Chd8* ablation in astroglia does not cause significant changes in basal transcription in the cortex of adult mice.

LPS induces a global neuroinflammatory state in the brain, which has been shown to trigger brain-wide changes in the transcriptional landscape mediated by epigenetic factors.[1,10,11] Both astrocytes and microglia are the major contributors to the brain's response to LPS insult, often through their reciprocal crosstalk.[3,65,66] We harvested cortical tissue 3 days post-LPS injections (Figure S10A) and performed bulk RNA-seq. Principal-component analysis revealed a robust effect of LPS administration (Figures S12A and S12B). In control mice, we identified 2,642 Differentially Expressed Genes (DEGs, FDR <0.05) that were introduced by LPS injection when compared to saline injection (Figures S12C and S12D). Gene Ontology (GO) analysis for upregulated genes revealed pathways associated with signal transduction and inflammatory processes such as regulation of cytokine production and myeloid cell differentiation and metabolic processes (Figures S12E and S12F; FDR < 0.05). These DEGs and pathways we detected from the LPS-treated control mice align well with findings from previous studies.[1,10,11,57,59,63,67,68]

When comparing LPS-treated control mice and LPS-treated astrocyte cKO mice, we identified a total of 109 DEGs between groups (FDR < 0.05; Figures 5A and 5B; Table S1). Among the 104 DEGs with reliable gene annotations, 41 genes were deemed to be astrocyte specific; 1 gene was categorized as microglia specific; and 4 genes were specific to neurons (Figure 5C), according to multiple previous reports.[67–69] Moreover, hypergeometric overrepresentation analysis between our dataset and datasets from previous studies[67–69] revealed robust enrichment for astrocytic genes with non-significant enrichment for other cell types (Figure 5D). We performed pathway analysis with the DEGs and categorized them into cellular pathways associated with cell metabolism, lipid homeostasis, and stress and secretory responses (Figure 5E). Interestingly, one of the pathways that emerged was response to cold (Figure 5E), coincidentally supporting our observation of atypical body-temperature response in astrocyte cKO mice after LPS injection (Figures 4N and 4O). Among the DEGs, we also identified genes, such as *Gstt3* (glutathione S-transferase, theta 3), that mediate signaling from astrocytes to microglia (Figure 5B; Table S1). *Gstt3* is downregulated in the astrocyte cKO group (Figure 5G), in which we found reduced microglia reactivity and neuroinflammation (Figure 4). Notably, a previous study demonstrated that

(D and E) High-magnification images of microglia from LPS-treated control (D) and LPS-treated astrocyte cKO mice (E) in the cortex, indicating the different reactive characteristics of Iba1$^+$ microglia.
(F and G) Representative skeletonized images of two microglia from control (F) and astrocyte cKO mice (G).
(H) Sholl analysis of microglia from both genotypes reveals a smaller number of intersections in microglia from astrocyte cKO mice (n = 40 cells from 3 mice per genotype).
(I) Decreased microglial cell territory volume after LPS treatment in astrocyte cKO mice.
(J) Reduced microglial cell volume in astrocyte cKO mice.
(K–M) Microglia from astrocyte cKO mice feature a reduced number of branchpoints (K) and endpoints (L) and maximum branch lengths (M).
(N) Typical temperature drop after LPS injection in control mice compared to saline-treated animals.
(O) Astrocyte cKO animals experience no drop in temperature compared to the saline-treated group after LPS administration.
(P) Survival curve depicting the observed mortality of controls after LPS injections. On the contrary, astrocyte cKO animals did not experience mortality (p = 0.0412, logrank [Mantel-Cox] test, n = 14 mice for control group; n = 16 mice for astrocyte cKO group).
In (A)–(C), scale bars indicate 200 μm; in (D) and (E), scale bars indicate 50 μm. In (H), asterisks indicate the range where the number of intersections is different, statistical analysis was performed with the mixed-effects model. In (I)–(M), *p < 0.05; **p < 0.01; ***p < 0.001; statistical analysis was carried out with the two-tailed Welch's t test; error bars indicate the SEM; data points represent n = 3 mice per genotype. Data points are normalized to the mean of each control group.

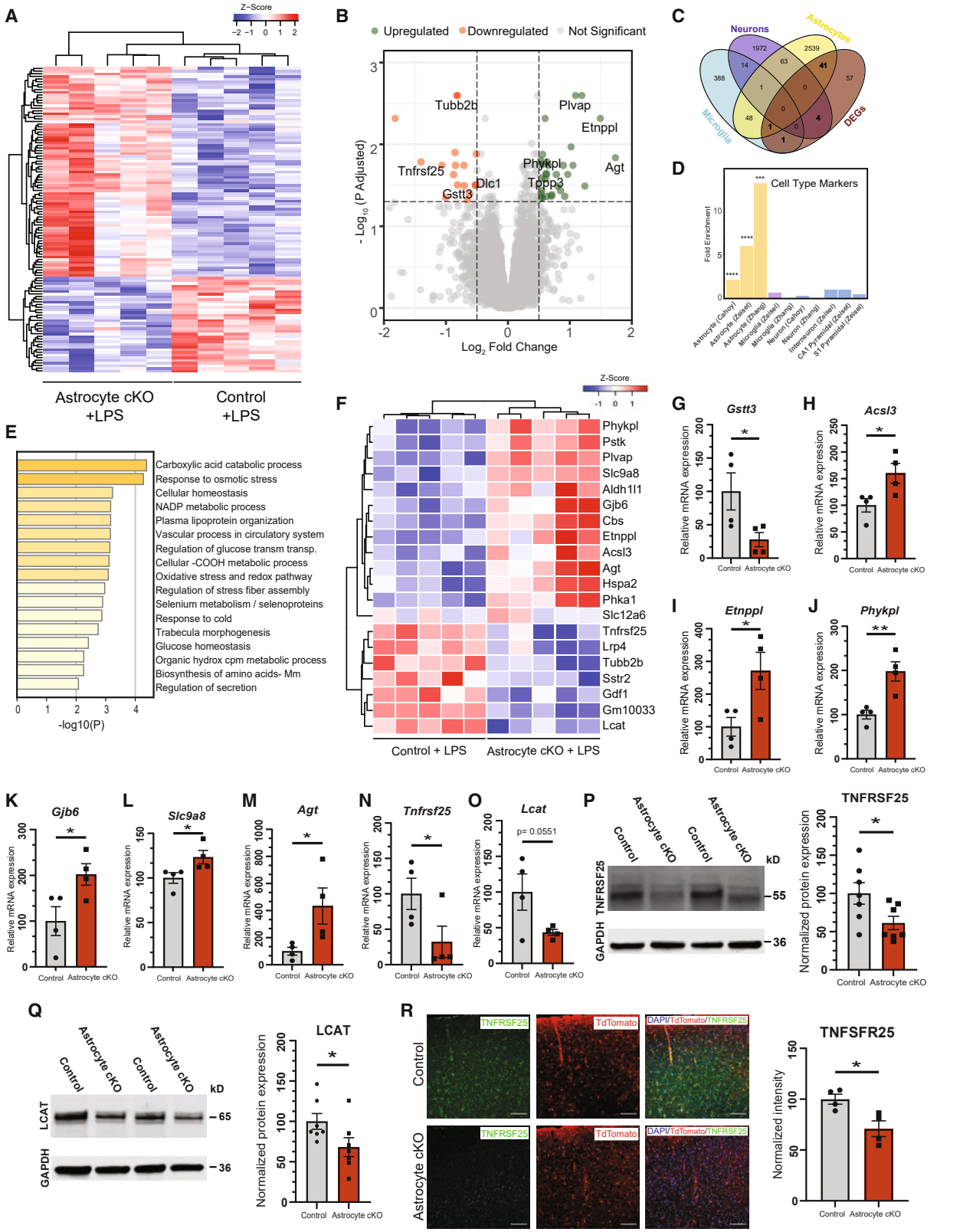

(legend on next page)

astrocyte-specific knockdown of *Gstt3* results in reduced microglia responses to LPS in the mouse brain.[70] These data indicate that CHD8 mediates important downstream pathways that are instrumental for astrocytes to microglia crosstalk during LPS.

We next verified genes from the top 20 ranked DEGs (Figure 5F), through real-time qPCR at the mRNA level and at the protein levels through western blotting and immunohistochemistry (Figures 5G–5R). For instance, we detected changes in genes that are involved in lipid (*Acsl3*, *Etnppl*, *Lcat*), amino acid (*Phykpl*), and ion (*Slc9a8*) synthesis and homeostasis; the CNS-astrocyte-specific gap junction protein (*Gjb6*)[68,71] and angiotensinogen (*Agt*)[72,73]; and the tumor necrosis factor receptor *Tnfrsf25* (Figures 5P and 5R). These genes have recently been shown to play a role in synuclein pathology,[74] fasting and neurological diseases,[75] amyotrophic lateral sclerosis (ALS),[76,77] neurodegeneration, alcohol abuse,[78] Alzheimer disease (AD),[79,80] multiple sclerosis (MS),[81] and Parkinson disease.[82] These results suggest that CHD8 mediates a number of vital transcriptional programs in astrocytes and regulates lipid-associated pathways and cellular homeostasis, which are pivotal to reactive gliosis and the brain's response to LPS-induced neuroinflammation.[10,72,83–85]

CHD8 regulates chromatin accessibility and transcription in astrocytes during LPS-induced neuroinflammation

Given the primary function of CHD8 as a chromatin regulator, we sought to examine the role of CHD8 in regulating the accessible chromatin landscape during neuroinflammation. We performed the assay for transposase-accessible chromatin with high-throughput sequencing (ATAC-seq) on astrocyte samples from adult mouse brains. We used magnetic activated cell sorting (MACS) to acquire astrocyte-enriched samples and detect changes in chromatin accessibility across experimental groups and treatments (Figure 6A). We identified high degrees of overlapped ATAC-seq peaks shared among groups (Figures 6B and 6C). We detected 1,789 differential peaks in LPS-treated control mice compared to the saline group (Figure 6B). Peak-calling revealed increases in accessibility in genomic regions such as enhancers and 3′ UTRs (Figure 6B). Comparing LPS-treated astrocyte cKO mice with LPS-treated controls, we detected bidirectional changes in accessibility in enhancers. Introns, intergenic regions, and promoters of genes displayed an increase in open chromatin in the astrocyte cKO group (Figure 6C). Similar to previous studies of *Chd8* mutations in other cell types, increased accessibility was observed in 5′ UTRs, introns, and non-coding RNA regions.[10,24,86] Collectively, our data revealed pronounced genome-wide changes in accessibility in astrocytes in the absence of CHD8 during LPS-induced neuroinflammation (Figure 6D). In parallel, we applied MACS to isolate and enrich microglia from the flowthrough after astrocyte purification to perform bulk RNA-seq (Figure S13). This independent RNA-seq from enriched microglia revealed four DEGs between LPS-treated control and LPS-treated astrocyte cKO mice (Figures S13I and S13J). Consistent with our tissue bulk RNA-seq data, we observed an effect on gene transcription in microglia that is modulated by astrocytic CHD8 during LPS-induced neuroinflammation.

We next juxtaposed the ATAC-seq dataset with the bulk tissue RNA-seq data (Figures 5A–5F). A number of differential peaks were detected proximally to DEGs, highlighting CHD8 as a modulator of their expression through chromatin remodeling (Figure 6E). Among them, upregulated and downregulated genes were associated with changes in the chromatin landscape, such as *Cbs* and *Gdf1*, respectively. Of those genes, many were found to be shared with published ATAC- and RNA-seq datasets from isolated astrocytes after LPS stimulation *in vivo*.[10,60] Among this convergent gene set, there are genes that encode for proteins involved in enzymatic processes (*Steap3*, *Adi*, *Ddc*, *Idh2*, *Adamts1*, *Stk40*), cellular morphology regulation (*Fat3*, *Lrrc8a*, *Calr*), and ion channels (*Kcnn2*). Several genes have previously been shown to have altered chromatin accessibility in *Chd8* KO, such as *Basp1*.[24] In our astrocyte samples, we find the loss of accessibility in the promoter region of genes such as *Basp1* (Figure 6F), similar to other studies with *Chd8* mutant NSCs.[24] We also detected

Figure 5. Transcriptional analysis of cortical tissues from control and astrocyte *Chd8* cKO mice after LPS administration

(A) Heatmap of DEGs identified through RNA-seq between control and astrocyte *Chd8* cKO mice after LPS treatment ($n = 5$ mice per genotype). A total of 109 DEGs were identified, 76 of which were upregulated and 33 were downregulated (FDR < 0.05).

(B) Volcano plot depicting the distribution of upregulated and downregulated genes, relative to their quantified fold change and their corresponding p values. The threshold was set at p (adjusted) < 0.05.

(C) Venn diagram of the detected DEGs, depicting a subset of DEGs that correspond to genes whose expression is specific to astrocytes, neurons, and microglia. Of those, many DEGs (41) were determined to be astrocyte specific, while fewer were deemed to be specific in neurons (4) and microglia (1).

(D) Bar plot showing the fold enrichment of the detected DEGs in our dataset, indicating significant enrichment of DEGs for astrocyte marker genes. Notably, no enrichment was detected when comparing neuronal or microglial genes to the cell-type markers from previous studies, as cited. ***$p < 0.001$; ****$p < 0.0001$.

(E) GO terms analysis reveals changes associated with many cellular processes, including lipid and metabolic pathways in astrocyte cKO mice in response to LPS stimulation.

(F) Heatmap of the top 20 DEGs identified through RNA-seq. Of these, 13 were upregulated and 7 were downregulated in astrocyte cKO mice treated with LPS vs. control mice treated with LPS.

(G–O) qPCR analysis of *Gstt3* (G), *Acsl3* (H), *Etnppl* (I), *Phykpl* (J), *Gjb6* (K), *Slc9a8* (L), *Agt* (M), *Tnfrsf25* (N), and *Lcat* (O) mRNA confirms the altered expression shown in (F) ($n = 4$ mice per group).

(P) Representative western blotting of TNFRSF25 from cortices of control and astrocyte cKO mice after LPS administration, showing reduced TNFRSF25 protein in the cortex of astrocyte cKO mice ($n = 7$ mice per group).

(Q) Representative western blotting of LCAT from cortices of control and astrocyte cKO mice after LPS administration showing reduced LCAT protein in astrocyte cKO mice ($n = 7$).

(R) Representative images of TNFRSF25 staining in the cortex of control and astrocyte cKO mice after LPS administration. Signal intensity quantification of TNFRSF25 staining ($n = 4$ mice per genotype). *$p < 0.05$; scale bars indicate 200 μm. Data points are normalized to the mean of the control group. Error bars depict the SEM. Statistical comparisons were performed with the one-tailed Welch's t test.

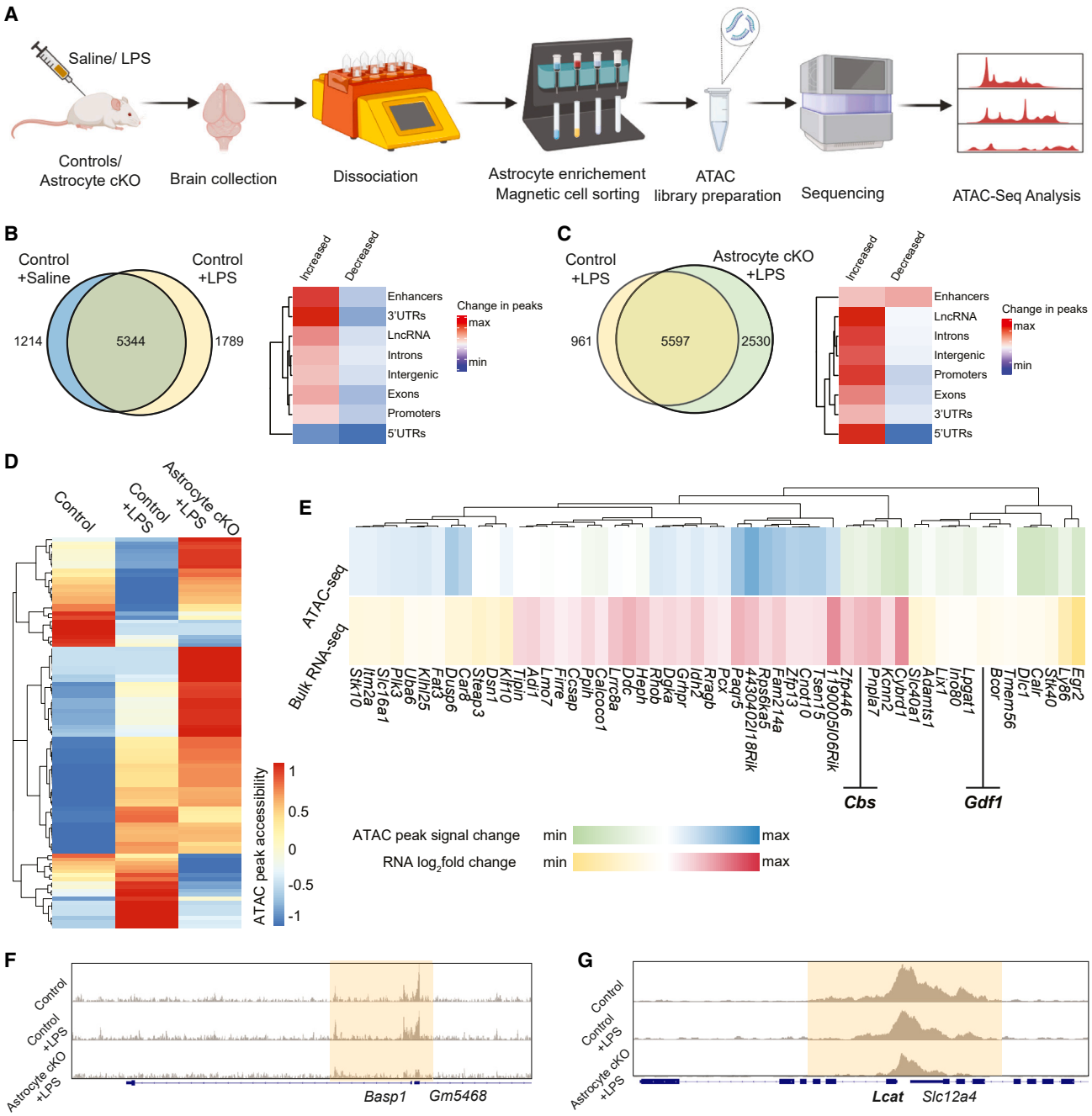

Figure 6. CHD8 mediates chromatin accessibility changes during LPS-induced neuroinflammation

(A) Flowchart of the experimental pipeline used to obtain astrocyte-enriched mouse brain samples for the subsequent ATAC-seq processing.

(B) Genomic annotation enrichment for altered (increased and decreased) chromatin accessibility between saline-treated control mice and LPS-treated control mice.

(C) Genomic annotation enrichment for altered (increased and decreased) chromatin accessibility between LPS-treated astrocyte cKO mice and LPS-treated control mice.

(D) Heatmap display of ATAC-seq deviations in chromatin accessibility across the three conditions.

(E) Heatmap representation of changes in ATAC-seq peaks near DEGs identified in our bulk RNA-seq experiments in Figure 5A.

(F and G) Representative genome tracks showing loss of accessibility proximal to transcription start sites of the *Basp1* gene identified in a previous study (F) and of the *Lcat* gene identified in our RNA-seq (G), in the astrocyte cKO samples.

reduced ATAC peaks in the promoter region of our identified DEGs (Figure 5F), such as the downregulated *Lcat*, in astrocytes (Figure 6G). Taken together, these data highlight the role of CHD8 in regulating chromatin accessibility in astrocytes, which orchestrates the expression of important regulators and cellular pathways during LPS-induced neuroinflammation.

AAV- and CRISPR-mediated direct *Chd8* editing in astrocytes *in vivo* attenuates reactive gliosis

Increased reactive gliosis represents one of the major hallmarks of various neurological conditions and diseases such as traumatic brain injury, stroke, AD, ALS, and MS.[1,3,5,10,83,84,87–90] As a result, reactive gliosis has recently been proposed as an emerging therapeutic target to tackle these complex and multifactorial conditions. Thus, we were motivated to find whether a translational approach that allows for direct, cell-type-specific *Chd8* ablation could mitigate reactive gliosis in the brain. Prompted by the pioneering work of others,[91–94] we engineered an AAV vector expressing a guide RNA (gRNA) targeting the *Chd8* gene and SaCas9 driven by the gfaABC$_1$D promoter (Figure 7A). We injected the scramble-AAV (control group) or *Chd8*-cKO-AAV (*Chd8*-cKO group) via stereotaxic injection into wild-type mice. The AAVs were administrated into the brain through the same Hamilton syringe with which we induced a stab. We assayed the expression of CHD8 in astrocytes and characterized reactive gliosis as described above (Figure 7B). We observed reduced expression of CHD8 in AAV-transduced (hemagglutinin [HA] tag$^+$) astrocytes (Sox9$^+$) expressing *Chd8*-cKO-gRNA as compared to scramble-gRNA-expressing controls (Figures 7C and 7D). Compared to scramble-AAV in the control group (Figure 7E), the *Chd8*-cKO-AAV group (Figure 7F) displays reduced GFAP but not Iba1 signals at the site of the injury (Figures 7G, 7H, S14, and S15A–S15D). Reactive astrocytes in the CRISPR-AAV-mediated *Chd8* cKO group showed a 15.75% decrease in GFAP$^+$ territory (Figure 7G), which is less than the 33.6% decrease in astrocyte-*Chd8* cKO mice (*Chd8*$^{fx/fx}$: *Aldh1l1-CreER*$^{T2+/-}$) (Figure 2H). The differential degree of reduction of reactive gliosis between the AAV-mediated *Chd8* cKO and the mouse genetic strategy (*Aldh1l1-CreER*^{T2}-mediated *Chd8* cKO) can be attributed to the fact that the genetic approach allows for sufficient time to ablate *Chd8* and remove the CHD8 protein from astrocytes prior to the stab-wound injury. Consistently, we observe a trend toward reduced morphological characteristics, including the territorial volume occupied by single astrocytes (Figure S15E), their cellular volume (Figure S15F), and ramification index (Figure S15G). These data demonstrate that an AAV-mediated *Chd8* gene ablation *in vivo* through CRISPR could be leveraged to mitigate reactive gliosis as a translatable approach against pathogenic neuroinflammation.

DISCUSSION

Excessive reactive gliosis and neuroinflammation have emerged as major factors in neurodegeneration, injury, epilepsy, and brain tumors.[1] There has been increasing interest and effort in deciphering the major transcriptional regulators responsible for converting glial cells to a reactive status in response to diverse pathogens.[10,11] Through the release of cytokines and signaling molecules, microglia and astrocytes share reciprocal crosstalk during reactive gliosis.[3,63,65,66,95] In this study, we characterized CHD8 in modulating reactive gliosis and neuroinflammation in the adult brain primarily through regulating chromatin accessibility and gene transcription in astrocytes. In the stab-wound injury model, we revealed that CHD8 in astrocytes regulates their proliferation and ability to acquire elongated and hypertrophic morphologies. These are typical responses of astrocytes to mechanical injury.[36,54] We found that ablating *Chd8* from astrocytes, but not microglia, resulted in a decrease of both astrocytes and microglia in the injury site, suggesting that the inherent crosstalk between the two cells is reliant on CHD8 in astrocytes. We further employed an LPS-induced inflammatory insult and uncovered that *Chd8* ablation in astrocytes results in an attenuated neuroinflammatory response, as indicated by reduced morphological changes in microglia and alleviated septic-associated hypothermia.[57,63] Our data underscore the critical role of CHD8-mediated epigenetic programming in astrocytes and its contribution to the crosstalk between astrocytes and microglia during neuroinflammation and reactive gliosis.

We further delineated the downstream pathways controlled by CHD8 in astrocytes during neuroinflammation. Our analysis of bulk RNA-seq data from LPS-treated mouse cortices identified an inventory of astrocyte-enriched pathways, a large percentage of which converged on lipid metabolism, the regulation of cellular homeostasis, and the response to stress signals. Indeed, lipid metabolism and transport and their effects on neuroinflammation have become a compelling topic, as implicated by recent studies.[84,96–98] One particularly notable recent study highlighted the relation between impaired fatty acid catabolism in the mitochondria of astrocytes and the aberrant neuroinflammation that can cause neurodegeneration.[99] Our transcriptional analysis identified genes such as *Etnppl*, *Gjb6*, *Phykpl*, *Agt*, and *Lcat* that were regulated by CHD8. These genes have been previously reported using single-cell approaches to be astrocyte enriched, crucial for gliosis, and associated with neurological conditions.[10,71–81,84,95,100] Interestingly, two of those genes (*Etnppl* and *Phykpl*) are mitochondrial genes that participate in fatty acid and amino acid degradation.[75,100] We found both *Etnppl* and *Phykpl* were upregulated after *Chd8* ablation in reactive astrocytes, providing potentially beneficial roles against LPS-induced neuroinflammation. Our results strengthen the notion that lipid metabolism in astrocytes is important in neuroinflammatory conditions, and identify CHD8 as a regulator of such pathways. Our transcriptional analysis also identified *Gstt3* to be controlled by CHD8 in astrocytes, which provides mechanistic insight into how the CHD8-mediated epigenetic programs facilitate astrocyte-to-microglia crosstalk during reactive gliosis. Finally, we probed the role of astrocytic CHD8 in regulating chromatin dynamics. Given the genome-wide, strong effects of CHD8 on chromatin accessibility, this calls for the investigation of other epigenetic regulators and ATP-chromatin remodeling factors, including other CHD family proteins, in reactive gliosis.

In humans, *CHD8* represents one of the most highly penetrant genes in ASD and other developmental disorders.[16,17,28,32,101–103] Clinical case studies have reported the association between

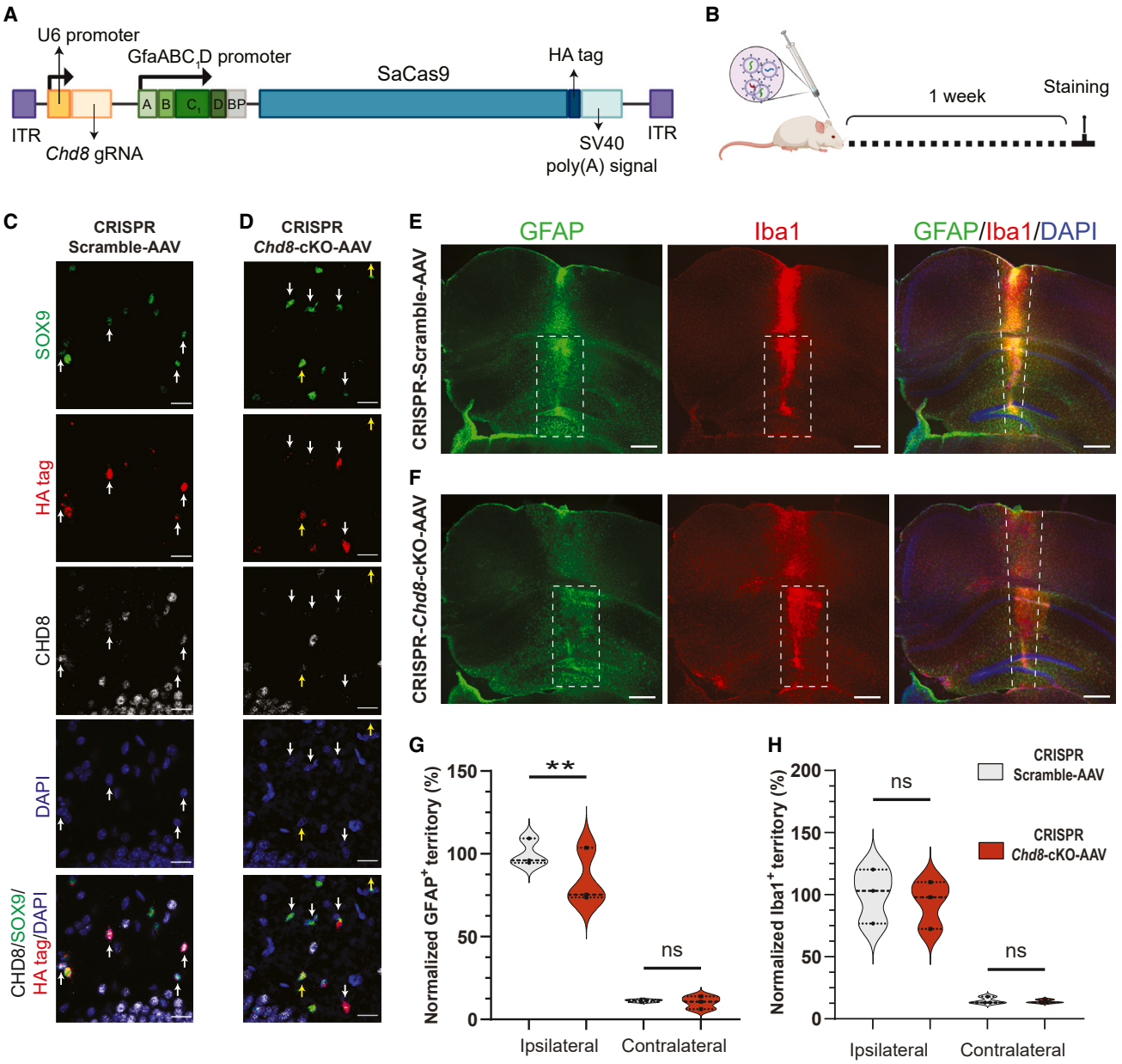

Figure 7. CRISPR-SaCas9-mediated *Chd8* editing through AAV in astrocytes mitigates reactive gliosis in the stab-wound injury model

(A) Schematic diagram illustrating the elements required for the designed AAV for astrocyte-specific *Chd8* editing *in vivo* via CRISPR-SaCas9.

(B) Diagram for the simultaneous AAV injection and stab-wound injury with analysis of reactive gliosis performed at 7 days post-injection.

(C) Representative images near the needle track from control mice (Scramble-AAV injected). CHD8 is detectable in astrocytes (SOX9$^+$) expressing SaCas9 (HA tag$^+$).

(D) Representative images near the needle track from mice injected with the *Chd8*-cKO AAVs. CHD8 is undetectable in the majority of HA$^+$ and SOX9$^+$ astrocytes (white arrows), while fewer HA$^+$ and SOX9$^+$ astrocytes still show CHD8 expression (yellow arrows).

(E and F) GFAP and Iba1 staining of astrocytes and microglia, respectively, after stab-wound injury and AAV injection in the Scramble-AAV (E) and *Chd8*-cKO-AAV groups (F).

(G) Decreased area occupied by GFAP$^+$ astrocytes in the *Chd8*-cKO-AAV mice.

(H) Quantification of the area occupied by Iba1$^+$ microglia between control and *Chd8*-cKO-AAV mice.

In (C) and (D), scale bars indicate 20 μm; in (E) and (F), scale bars indicate 500 μm. The dashed rectangle indicates the ROIs that were quantified in (G) and (H). The dashed lines in merged images indicate the needle track of the injury. In (G) and (H), statistical comparisons were performed with two-way ANOVA; $^{**}p < 0.01$. Data points indicate $n = 3$ mice per group. Data are normalized to the means of the ipsilateral site in the control group.

neuroinflammation and ASD, with pro-inflammatory cytokines and chemokines being elevated in biopsies and brain tissues from some affected individuals.[104–106] Our findings on *Chd8* in reactive gliosis and neuroinflammation provide an entry point and a window to further dissect the complex interactions among gene mutations, neuroinflammation, atypical brain development, and ASD. Neuroinflammation is a recurring and common brain pathophysiology that underlies a wide variety of neurological diseases.[1] Progress from basic and clinical neuroscience has established the toxic effects of reactive gliosis in some of these conditions and its potential for therapeutic intervention.[107–109]

In conclusion, we discovered that CHD8, a chromatin remodeler and a causal gene for ASD and neurodevelopmental disorders, is a mediator of injury- and LPS-triggered reactive gliosis and neuroinflammation in the adult mouse brain, through chromatin remodeling and transcriptional control in astrocytes. Beneficially modulating reactive astrocytes in injury and neurological conditions holds promise as a direction for mitigating disease-associated pathophysiology.[10,44,110] We extended the findings from mouse genetics to an AAV-mediated *in vivo* gene editing approach. This study presents compelling evidence on epigenetic mechanisms involved in reactive gliosis and highlights their potential as targets for ameliorating neuroinflammation in injury and disease. Our findings provide insight into the biological functions of ASD-associated genes in the adult brain and reveal the potential for harnessing these mechanisms for translational applications.

Limitations of the study

We note some limitations of our study that could be addressed in future work toward a deeper mechanistic understanding and the functional implications. First, we recognize reactive gliosis and the interplay between astrocytes and microglia to be highly dynamic and dependent on diverse subpopulations of these cells that elicit discreet responses to inflammatory stimuli.[1,2,10,111,112] Future efforts using improved tools to study astrocytes and single-cell RNA-seq could help to gain insight into transcriptionally distinct subpopulations and address the heterogeneity of astrocytes and other cells involved in reactive gliosis.[10,84,113,114] Second, we utilized stab-wound injury and LPS as two representative paradigms; however, we cannot exclude the possibility that CHD8 might exert differential roles on reactive gliosis in other models and conditions associated with injury and neuroinflammation.[1,115,116] We did not elaborate on the functional impact of reduced gliosis on neurons, neural circuits, or the pathophysiology of the brain, which could be examined in disease models such as stroke, epilepsy, brain tumors, spinal cord injury, neuropsychiatric disorders, neurodevelopment, and neurodegeneration.[1,4,7,117] Third, while our study offers a thorough cellular and functional dissection of *Chd8* in mice, these findings need to be validated in higher-order organisms, such as non-human primates and postmortem human brains, for a faithful translation to reactive gliosis in human neurological diseases. Additionally, various models of glial cells derived from patient iPSCs could also be applied to revisit the function of CHD8 and other epigenetic factors in astrocytes in the context of human disease.[95,98]

STAR★METHODS

Detailed methods are provided in the online version of this paper and include the following:

- KEY RESOURCES TABLE
- RESOURCE AVAILABILITY
  - Lead contact
  - Materials availability
  - Data and code availability
- EXPERIMENTAL MODEL AND STUDY PARTICIPANT DETAILS
- METHOD DETAILS
  - Tamoxifen preparation and feeding
  - Viral vectors, *in vivo* gene editing, and surgical procedures on mice
  - Immunohistochemistry and imaging of brain slices
  - Reactive gliosis quantification for the "stab-wound" injury method
  - Assay of astrocyte proliferation *in vivo*
  - Sholl analysis and characterization of cell morphology
  - LPS administration
  - Behavioral assessments
  - Western blotting and protein quantification
  - RNA isolation and real-time Q-PCR assay
  - Bulk RNA sequencing and analytic pipeline
  - Differential expressed genes (DEGs) analysis
  - Enrichment analysis
  - Isolation of astrocytes and microglia from adult mouse brains
  - RNA-seq library preparation and analysis for microglia-enriched samples
  - ATAC-seq library preparation and analysis of differential open chromatin
- QUANTIFICATION AND STATISTICAL ANALYSIS

SUPPLEMENTAL INFORMATION

Supplemental information can be found online at https://doi.org/10.1016/j.celrep.2024.114637.

ACKNOWLEDGMENTS

We thank Dr. Simon Chen, Dr. Salvatore Carbonetto, and Dr. Wayne S. Sossin for their comments and critical reading of the manuscript. We thank Ms. Marjorie Allison Bergeron from Miltenyi Biotec for excellent technical support on tissue dissociation and MACS experiments. We are grateful to the generous funding support from the following sources to Y.Z.: the NSERC Discovery Grants (RGPIN-2020-04872 and DGECR-2020-00030), the Djavad Mowafaghian Foundation, the NARSAD Young Investigator Grant (2021) from the Brain & Behavior Research Foundation, and the Douglas Avrith University of Cambridge/Montreal Neurological Institute-Hospital Neuroscience Collaboration (2023), Canada Research Chair (Tier II) program, The John R. Evans Leaders Fund from CFI (project no. 38264), the Azrieli Center for Autism Research (ACAR), The Azrieli Foundation, the New Investigator Grant (no. NI22-1106) from the SickKids Foundation, and a Canadian Institutes of Health Research Project Grant (PJT no. 191866). This research was undertaken thanks, in part, to funding from the Canada First Research Excellence Fund, awarded to McGill University for the Healthy Brains for Healthy Lives initiative. R.E.Y. and N.E.S. are supported by the Simons Foundation for Autism Research (Genomics of ASD 896724). T.I. was supported by grants (P41 GM103504 and U01 MH115747) from the NIH. Y.M. was supported by the F32 Postdoctoral Fellowship from the National Institute of Mental Health. P.M. was supported by a fellowship from the National Research Training Platform in Neurodevelopmental Disorders through Transforming Autism Care Consortium (now CanNRT) in 2022, a fellowship from the Healthy Brains for Healthy Lives initiative in 2023, and Fonds de recherche du Québec-Santé (FRQS), Formation de doctorat from 2024 to 2027. R.S. was supported by the Molson Neuro-Engineering Award from IPN/The Neuro in 2021 and a doctoral fellowship (2023–2026) from the Canadian Institutes of Health

Research through the CGS-D program. All cartoon diagrams in the graphical abstract, figures, and supplemental figures were created with BioRender.com.

AUTHOR CONTRIBUTIONS

P.M. and Y.Z. conceived the study. Y.Z., P.M., J.J.W., L.Y., G.F., W.T.F., and K.K.M. generated, collected, and characterized the mouse strains. P.M., X.T., L.Y., R.S., and T.K. performed the animal, surgical, imaging, RNA-seq, mRNA, and protein experiments. P.M., R.S., and Y.Z. performed the *in vivo* gene editing experiments. Y.M., P.M., and T.I. performed the transcriptional analysis. R.E.Y., P.M., and Y.Z. performed experiments for ATAC-seq and data analysis. K.C. and A.K. contributed to imaging collection and data analysis. H.E., W.T.F., K.C., P.U.L., B.A.Y., H.C., D.R., T.K., and P.D. participated in experiments and contributed to data collection and analysis. P.D., S.S., K.P., G.W.Y., K.K.M., G.F., G.A.R., T.I., and N.E.S. provided critical input on the experimental design and direction guidance at various stages. K.K.M., G.F., and G.A.R. contributed to discussions and reviews of the manuscript. P.M. and Y.Z. wrote the manuscript, with input from other authors.

DECLARATION OF INTERESTS

T.I. is a co-founder, member of the advisory board, and has an equity interest in Data4Cure and Serinus Biosciences. He is a consultant for and has an equity interest in Ideaya BioSciences and Light Horse Therapeutics. The terms of these arrangements have been reviewed and approved by University of California, San Diego in accordance with its conflict of interest policies. N.E.S. is an adviser to Qiagen and a co-founder of and adviser to TruEdit Bio and OverT Bio.

Received: September 25, 2023
Revised: June 11, 2024
Accepted: July 30, 2024

REFERENCES

1. Burda, J.E., and Sofroniew, M.V. (2014). Reactive gliosis and the multicellular response to CNS damage and disease. Neuron *81*, 229–248. https://doi.org/10.1016/j.neuron.2013.12.034.
2. Escartin, C., Galea, E., Lakatos, A., O'Callaghan, J.P., Petzold, G.C., Serrano-Pozo, A., Steinhäuser, C., Volterra, A., Carmignoto, G., Agarwal, A., et al. (2021). Reactive astrocyte nomenclature, definitions, and future directions. Nat. Neurosci. *24*, 312–325. https://doi.org/10.1038/s41593-020-00783-4.
3. Liddelow, S.A., Guttenplan, K.A., Clarke, L.E., Bennett, F.C., Bohlen, C.J., Schirmer, L., Bennett, M.L., Münch, A.E., Chung, W.S., Peterson, T.C., et al. (2017). Neurotoxic reactive astrocytes are induced by activated microglia. Nature *541*, 481–487. https://doi.org/10.1038/nature21029.
4. Burda, J.E., Bernstein, A.M., and Sofroniew, M.V. (2016). Astrocyte roles in traumatic brain injury. Exp. Neurol. *275*, 305–315. https://doi.org/10.1016/j.expneurol.2015.03.020.
5. Yiu, G., and He, Z. (2006). Glial inhibition of CNS axon regeneration. Nat. Rev. Neurosci. *7*, 617–627. https://doi.org/10.1038/nrn1956.
6. Brambilla, R., Bracchi-Ricard, V., Hu, W.H., Frydel, B., Bramwell, A., Karmally, S., Green, E.J., and Bethea, J.R. (2005). Inhibition of astroglial nuclear factor kappaB reduces inflammation and improves functional recovery after spinal cord injury. J. Exp. Med. *202*, 145–156. https://doi.org/10.1084/jem.20041918.
7. Wanner, I.B., Anderson, M.A., Song, B., Levine, J., Fernandez, A., Gray-Thompson, Z., Ao, Y., and Sofroniew, M.V. (2013). Glial scar borders are formed by newly proliferated, elongated astrocytes that interact to corral inflammatory and fibrotic cells via STAT3-dependent mechanisms after spinal cord injury. J. Neurosci. *33*, 12870–12886. https://doi.org/10.1523/JNEUROSCI.2121-13.2013.
8. Sirko, S., Behrendt, G., Johansson, P.A., Tripathi, P., Costa, M., Bek, S., Heinrich, C., Tiedt, S., Colak, D., Dichgans, M., et al. (2013). Reactive glia in the injured brain acquire stem cell properties in response to sonic hedgehog. Cell Stem Cell *12*, 426–439, [corrected]. https://doi.org/10.1016/j.stem.2013.01.019.
9. Li, W., Shan, B., Zou, C., Wang, H., Zhang, M.M., Zhu, H., Naito, M.G., Xu, D., Manuel, V.J., Mifflin, L., et al. (2022). Nuclear RIPK1 promotes chromatin remodeling to mediate inflammatory response. Cell Res. *32*, 621–637. https://doi.org/10.1038/s41422-022-00673-3.
10. Burda, J.E., O'Shea, T.M., Ao, Y., Suresh, K.B., Wang, S., Bernstein, A.M., Chandra, A., Deverasetty, S., Kawaguchi, R., Kim, J.H., et al. (2022). Divergent transcriptional regulation of astrocyte reactivity across disorders. Nature *606*, 557–564. https://doi.org/10.1038/s41586-022-04739-5.
11. Leng, K., Rose, I.V.L., Kim, H., Xia, W., Romero-Fernandez, W., Rooney, B., Koontz, M., Li, E., Ao, Y., Wang, S., et al. (2022). CRISPRi screens in human iPSC-derived astrocytes elucidate regulators of distinct inflammatory reactive states. Nat. Neurosci. *25*, 1528–1542. https://doi.org/10.1038/s41593-022-01180-9.
12. Koreman, E., Sun, X., and Lu, Q.R. (2018). Chromatin remodeling and epigenetic regulation of oligodendrocyte myelination and myelin repair. Mol. Cell. Neurosci. *87*, 18–26. https://doi.org/10.1016/j.mcn.2017.11.010.
13. Sheehan, P.W., Nadarajah, C.J., Kanan, M.F., Patterson, J.N., Novotny, B., Lawrence, J.H., King, M.W., Brase, L., Inman, C.E., Yuede, C.M., et al. (2023). An astrocyte BMAL1-BAG3 axis protects against alpha-synuclein and tau pathology. Neuron *111*, 2383–2398.e7. https://doi.org/10.1016/j.neuron.2023.05.006.
14. Williamson, M.R., Fuertes, C.J.A., Dunn, A.K., Drew, M.R., and Jones, T.A. (2021). Reactive astrocytes facilitate vascular repair and remodeling after stroke. Cell Rep. *35*, 109048. https://doi.org/10.1016/j.celrep.2021.109048.
15. Amir, R.E., Van den Veyver, I.B., Wan, M., Tran, C.Q., Francke, U., and Zoghbi, H.Y. (1999). Rett syndrome is caused by mutations in X-linked MECP2, encoding methyl-CpG-binding protein 2. Nat. Genet. *23*, 185–188. https://doi.org/10.1038/13810.
16. O'Roak, B.J., Vives, L., Fu, W., Egertson, J.D., Stanaway, I.B., Phelps, I.G., Carvill, G., Kumar, A., Lee, C., Ankenman, K., et al. (2012). Multiplex targeted sequencing identifies recurrently mutated genes in autism spectrum disorders. Science *338*, 1619–1622. https://doi.org/10.1126/science.1227764.
17. Bernier, R., Golzio, C., Xiong, B., Stessman, H.A., Coe, B.P., Penn, O., Witherspoon, K., Gerdts, J., Baker, C., Vulto-van Silfhout, A.T., et al. (2014). Disruptive CHD8 mutations define a subtype of autism early in development. Cell *158*, 263–276. https://doi.org/10.1016/j.cell.2014.06.017.
18. Kadoch, C., and Crabtree, G.R. (2015). Mammalian SWI/SNF chromatin remodeling complexes and cancer: Mechanistic insights gained from human genomics. Sci. Adv. *1*, e1500447. https://doi.org/10.1126/sciadv.1500447.
19. Kerschbamer, E., Arnoldi, M., Tripathi, T., Pellegrini, M., Maturi, S., Erdin, S., Salviato, E., Di Leva, F., Sebestyén, E., Dassi, E., et al. (2022). CHD8 suppression impacts on histone H3 lysine 36 trimethylation and alters RNA alternative splicing. Nucleic Acids Res. *50*, 12809–12828. https://doi.org/10.1093/nar/gkac1134.
20. Konev, A.Y., Tribus, M., Park, S.Y., Podhraski, V., Lim, C.Y., Emelyanov, A.V., Vershilova, E., Pirrotta, V., Kadonaga, J.T., Lusser, A., and Fyodorov, D.V. (2007). CHD1 motor protein is required for deposition of histone variant H3.3 into chromatin in vivo. Science *317*, 1087–1090. https://doi.org/10.1126/science.1145339.
21. Micucci, J.A., Sperry, E.D., and Martin, D.M. (2015). Chromodomain helicase DNA-binding proteins in stem cells and human developmental diseases. Stem Cells Dev. *24*, 917–926. https://doi.org/10.1089/scd.2014.0544.

22. Hargreaves, D.C., and Crabtree, G.R. (2011). ATP-dependent chromatin remodeling: genetics, genomics and mechanisms. Cell Res. *21*, 396–420. https://doi.org/10.1038/cr.2011.32.

23. Ishihara, K., Oshimura, M., and Nakao, M. (2006). CTCF-dependent chromatin insulator is linked to epigenetic remodeling. Mol. Cell *23*, 733–742. https://doi.org/10.1016/j.molcel.2006.08.008.

24. Sood, S., Weber, C.M., Hodges, H.C., Krokhotin, A., Shalizi, A., and Crabtree, G.R. (2020). CHD8 dosage regulates transcription in pluripotency and early murine neural differentiation. Proc. Natl. Acad. Sci. USA *117*, 22331–22340. https://doi.org/10.1073/pnas.1921963117.

25. Zhao, C., Dong, C., Frah, M., Deng, Y., Marie, C., Zhang, F., Xu, L., Ma, Z., Dong, X., Lin, Y., et al. (2018). Dual Requirement of CHD8 for Chromatin Landscape Establishment and Histone Methyltransferase Recruitment to Promote CNS Myelination and Repair. Dev. Cell *45*, 753–768.e8. https://doi.org/10.1016/j.devcel.2018.05.022.

26. Coll-Tane, M., Gong, N.N., Belfer, S.J., van Renssen, L.V., Kurtz-Nelson, E.C., Szuperak, M., Eidhof, I., van Reijmersdal, B., Terwindt, I., Durkin, J., et al. (2021). The CHD8/CHD7/Kismet family links blood-brain barrier glia and serotonin to ASD-associated sleep defects. Sci. Adv. *7*, eabe2626. https://doi.org/10.1126/sciadv.abe2626.

27. Gompers, A.L., Su-Feher, L., Ellegood, J., Copping, N.A., Riyadh, M.A., Stradleigh, T.W., Pride, M.C., Schaffler, M.D., Wade, A.A., Catta-Preta, R., et al. (2017). Germline Chd8 haploinsufficiency alters brain development in mouse. Nat. Neurosci. *20*, 1062–1073. https://doi.org/10.1038/nn.4592.

28. Katayama, Y., Nishiyama, M., Shoji, H., Ohkawa, Y., Kawamura, A., Sato, T., Suyama, M., Takumi, T., Miyakawa, T., and Nakayama, K.I. (2016). CHD8 haploinsufficiency results in autistic-like phenotypes in mice. Nature *537*, 675–679. https://doi.org/10.1038/nature19357.

29. Villa, C.E., Cheroni, C., Dotter, C.P., López-Tóbon, A., Oliveira, B., Sacco, R., Yahya, A.Ç., Morandell, J., Gabriele, M., Tavakoli, M.R., et al. (2022). CHD8 haploinsufficiency links autism to transient alterations in excitatory and inhibitory trajectories. Cell Rep. *39*, 110615. https://doi.org/10.1016/j.celrep.2022.110615.

30. Atsuki Kawamura, Y.K., Kakegawa, W., Ino, D., Nishiyama, M., Yuzaki, M., and Nakayama, K.I. (2021). The autism-associated protein CHD8 is required for cerebellar development and motor function. Cell Rep. *35*, 108932.

31. Kweon, H., Jung, W.B., Im, G.H., Ryoo, J., Lee, J.H., Do, H., Choi, Y., Song, Y.H., Jung, H., Park, H., et al. (2021). Excitatory neuronal CHD8 in the regulation of neocortical development and sensory-motor behaviors. Cell Rep. *34*, 108780. https://doi.org/10.1016/j.celrep.2021.108780.

32. Platt, R.J., Zhou, Y., Slaymaker, I.M., Shetty, A.S., Weisbach, N.R., Kim, J.A., Sharma, J., Desai, M., Sood, S., Kempton, H.R., et al. (2017). Chd8 Mutation Leads to Autistic-like Behaviors and Impaired Striatal Circuits. Cell Rep. *19*, 335–350. https://doi.org/10.1016/j.celrep.2017.03.052.

33. Guo, C., Yang, W., and Lobe, C.G. (2002). A Cre recombinase transgene with mosaic, widespread tamoxifen-inducible action. Genesis *32*, 8–18. https://doi.org/10.1002/gene.10021.

34. Mei, Y., Monteiro, P., Zhou, Y., Kim, J.A., Gao, X., Fu, Z., and Feng, G. (2016). Adult restoration of Shank3 expression rescues selective autistic-like phenotypes. Nature *530*, 481–484. https://doi.org/10.1038/nature16971.

35. Buffo, A., Rite, I., Tripathi, P., Lepier, A., Colak, D., Horn, A.P., Mori, T., and Götz, M. (2008). Origin and progeny of reactive gliosis: A source of multipotent cells in the injured brain. Proc. Natl. Acad. Sci. USA *105*, 3581–3586. https://doi.org/10.1073/pnas.0709002105.

36. Robel, S., Bardehle, S., Lepier, A., Brakebusch, C., and Götz, M. (2011). Genetic deletion of cdc42 reveals a crucial role for astrocyte recruitment to the injury site in vitro and in vivo. J. Neurosci. *31*, 12471–12482. https://doi.org/10.1523/JNEUROSCI.2696-11.2011.

37. Cernak, I. (2005). Animal models of head trauma. NeuroRx *2*, 410–422. https://doi.org/10.1602/neurorx.2.3.410.

38. Theodoric, N., Bechberger, J.F., Naus, C.C., and Sin, W.C. (2012). Role of gap junction protein connexin43 in astrogliosis induced by brain injury. PLoS One *7*, e47311. https://doi.org/10.1371/journal.pone.0047311.

39. Norazit, A., Nguyen, M.N., Dickson, C.G.M., Tuxworth, G., Goss, B., Mackay-Sim, A., and Meedeniya, A.C.B. (2011). Vascular endothelial growth factor and platelet derived growth factor modulates the glial response to a cortical stab injury. Neuroscience *192*, 652–660. https://doi.org/10.1016/j.neuroscience.2011.06.035.

40. Bennett, M.L., Bennett, F.C., Liddelow, S.A., Ajami, B., Zamanian, J.L., Fernhoff, N.B., Mulinyawe, S.B., Bohlen, C.J., Adil, A., Tucker, A., et al. (2016). New tools for studying microglia in the mouse and human CNS. Proc. Natl. Acad. Sci. USA *113*, E1738–E1746. https://doi.org/10.1073/pnas.1525528113.

41. Ortinski, P.I., Dong, J., Mungenast, A., Yue, C., Takano, H., Watson, D.J., Haydon, P.G., and Coulter, D.A. (2010). Selective induction of astrocytic gliosis generates deficits in neuronal inhibition. Nat. Neurosci. *13*, 584–591. https://doi.org/10.1038/nn.2535.

42. Pekny, M., and Nilsson, M. (2005). Astrocyte activation and reactive gliosis. Glia *50*, 427–434. https://doi.org/10.1002/glia.20207.

43. Srinivasan, R., Lu, T.Y., Chai, H., Xu, J., Huang, B.S., Golshani, P., Coppola, G., and Khakh, B.S. (2016). New Transgenic Mouse Lines for Selectively Targeting Astrocytes and Studying Calcium Signals in Astrocyte Processes In Situ and In Vivo. Neuron *92*, 1181–1195. https://doi.org/10.1016/j.neuron.2016.11.030.

44. Wheeler, M.A., Clark, I.C., Tjon, E.C., Li, Z., Zandee, S.E.J., Couturier, C.P., Watson, B.R., Scalisi, G., Alkwai, S., Rothhammer, V., et al. (2020). MAFG-driven astrocytes promote CNS inflammation. Nature *578*, 593–599. https://doi.org/10.1038/s41586-020-1999-0.

45. Lee, J.H., Kim, J.Y., Noh, S., Lee, H., Lee, S.Y., Mun, J.Y., Park, H., and Chung, W.S. (2021). Astrocytes phagocytose adult hippocampal synapses for circuit homeostasis. Nature *590*, 612–617. https://doi.org/10.1038/s41586-020-03060-3.

46. Wang, C., Xiong, M., Gratuze, M., Bao, X., Shi, Y., Andhey, P.S., Manis, M., Schroeder, C., Yin, Z., Madore, C., et al. (2021). Selective removal of astrocytic APOE4 strongly protects against tau-mediated neurodegeneration and decreases synaptic phagocytosis by microglia. Neuron *109*, 1657–1674.e7. https://doi.org/10.1016/j.neuron.2021.03.024.

47. Stogsdill, J.A., Ramirez, J., Liu, D., Kim, Y.H., Baldwin, K.T., Enustun, E., Ejikeme, T., Ji, R.R., and Eroglu, C. (2017). Astrocytic neuroligins control astrocyte morphogenesis and synaptogenesis. Nature *551*, 192–197. https://doi.org/10.1038/nature24638.

48. Stringer, C., Wang, T., Michaelos, M., and Pachitariu, M. (2021). Cellpose: a generalist algorithm for cellular segmentation. Nat. Methods *18*, 100–106. https://doi.org/10.1038/s41592-020-01018-x.

49. Oltmer, J., Rosenblum, E.W., Williams, E.M., Roy, J., Llamas-Rodriguez, J., Perosa, V., Champion, S.N., Frosch, M.P., and Augustinack, J.C. (2023). Stereology neuron counts correlate with deep learning estimates in the human hippocampal subregions. Sci. Rep. *13*, 5884. https://doi.org/10.1038/s41598-023-32903-y.

50. Loane, D.J., and Byrnes, K.R. (2010). Role of microglia in neurotrauma. Neurotherapeutics *7*, 366–377. https://doi.org/10.1016/j.nurt.2010.07.002.

51. Kaiser, T., and Feng, G. (2019). Tmem119-EGFP and Tmem119-CreERT2 Transgenic Mice for Labeling and Manipulating Microglia. eNeuro *6*. https://doi.org/10.1523/ENEURO.0448-18.2019.

52. Absinta, M., Maric, D., Gharagozloo, M., Garton, T., Smith, M.D., Jin, J., Fitzgerald, K.C., Song, A., Liu, P., Lin, J.P., et al. (2021). A lymphocyte-microglia-astrocyte axis in chronic active multiple sclerosis. Nature *597*, 709–714. https://doi.org/10.1038/s41586-021-03892-7.

53. Tansley, S., Gu, N., Guzmán, A.U., Cai, W., Wong, C., Lister, K.C., Muñoz-Pino, E., Yousefpour, N., Roome, R.B., Heal, J., et al. (2022). Microglia-mediated degradation of perineuronal nets promotes pain. Science *377*, 80–86. https://doi.org/10.1126/science.abl6773.

54. Bardehle, S., Krüger, M., Buggenthin, F., Schwausch, J., Ninkovic, J., Clevers, H., Snippert, H.J., Theis, F.J., Meyer-Luehmann, M., Bechmann, I., et al. (2013). Live imaging of astrocyte responses to acute injury reveals selective juxtavascular proliferation. Nat. Neurosci. *16*, 580–586. https://doi.org/10.1038/nn.3371.

55. York, E.M., LeDue, J.M., Bernier, L.P., and MacVicar, B.A. (2018). 3DMorph Automatic Analysis of Microglial Morphology in Three Dimensions from Ex Vivo and In Vivo Imaging. eNeuro *5*. https://doi.org/10.1523/ENEURO.0266-18.2018.

56. Bernier, L.P., York, E.M., Kamyabi, A., Choi, H.B., Weilinger, N.L., and MacVicar, B.A. (2020). Microglial metabolic flexibility supports immune surveillance of the brain parenchyma. Nat. Commun. *11*, 1559. https://doi.org/10.1038/s41467-020-15267-z.

57. Zamanian, J.L., Xu, L., Foo, L.C., Nouri, N., Zhou, L., Giffard, R.G., and Barres, B.A. (2012). Genomic analysis of reactive astrogliosis. J. Neurosci. *32*, 6391–6410. https://doi.org/10.1523/JNEUROSCI.6221-11.2012.

58. Qin, L., Wu, X., Block, M.L., Liu, Y., Breese, G.R., Hong, J.S., Knapp, D.J., and Crews, F.T. (2007). Systemic LPS causes chronic neuroinflammation and progressive neurodegeneration. Glia *55*, 453–462. https://doi.org/10.1002/glia.20467.

59. Skelly, D.T., Hennessy, E., Dansereau, M.A., and Cunningham, C. (2013). A systematic analysis of the peripheral and CNS effects of systemic LPS, IL-1beta, [corrected] TNF-alpha and IL-6 challenges in C57BL/6 mice. PLoS One *8*, e69123. https://doi.org/10.1371/journal.pone.0069123.

60. Diaz-Castro, B., Bernstein, A.M., Coppola, G., Sofroniew, M.V., and Khakh, B.S. (2021). Molecular and functional properties of cortical astrocytes during peripherally induced neuroinflammation. Cell Rep. *36*, 109508. https://doi.org/10.1016/j.celrep.2021.109508.

61. Vainchtein, I.D., and Molofsky, A.V. (2020). Astrocytes and Microglia: In Sickness and in Health. Trends Neurosci. *43*, 144–154. https://doi.org/10.1016/j.tins.2020.01.003.

62. Meneses, G., Rosetti, M., Espinosa, A., Florentino, A., Bautista, M., Díaz, G., Olvera, G., Bárcena, B., Fleury, A., Adalid-Peralta, L., et al. (2018). Recovery from an acute systemic and central LPS-inflammation challenge is affected by mouse sex and genetic background. PLoS One *13*, e0201375. https://doi.org/10.1371/journal.pone.0201375.

63. Norden, D.M., Trojanowski, P.J., Villanueva, E., Navarro, E., and Godbout, J.P. (2016). Sequential activation of microglia and astrocyte cytokine expression precedes increased Iba-1 or GFAP immunoreactivity following systemic immune challenge. Glia *64*, 300–316. https://doi.org/10.1002/glia.22930.

64. Mei, J., Riedel, N., Grittner, U., Endres, M., Banneke, S., and Emmrich, J.V. (2018). Body temperature measurement in mice during acute illness: implantable temperature transponder versus surface infrared thermometry. Sci. Rep. *8*, 3526. https://doi.org/10.1038/s41598-018-22020-6.

65. Rothhammer, V., Borucki, D.M., Tjon, E.C., Takenaka, M.C., Chao, C.C., Ardura-Fabregat, A., de Lima, K.A., Gutiérrez-Vázquez, C., Hewson, P., Staszewski, O., et al. (2018). Microglial control of astrocytes in response to microbial metabolites. Nature *557*, 724–728. https://doi.org/10.1038/s41586-018-0119-x.

66. Clark, D.P.Q., Perreau, V.M., Shultz, S.R., Brady, R.D., Lei, E., Dixit, S., Taylor, J.M., Beart, P.M., and Boon, W.C. (2019). Inflammation in Traumatic Brain Injury: Roles for Toxic A1 Astrocytes and Microglial-Astrocytic Crosstalk. Neurochem. Res. *44*, 1410–1424. https://doi.org/10.1007/s11064-019-02721-8.

67. Cahoy, J.D., Emery, B., Kaushal, A., Foo, L.C., Zamanian, J.L., Christopherson, K.S., Xing, Y., Lubischer, J.L., Krieg, P.A., Krupenko, S.A., et al. (2008). A transcriptome database for astrocytes, neurons, and oligodendrocytes: a new resource for understanding brain development and function. J. Neurosci. *28*, 264–278. https://doi.org/10.1523/JNEUROSCI.4178-07.2008.

68. Zhang, Y., Chen, K., Sloan, S.A., Bennett, M.L., Scholze, A.R., O'Keeffe, S., Phatnani, H.P., Guarnieri, P., Caneda, C., Ruderisch, N., et al. (2014). An RNA-sequencing transcriptome and splicing database of glia, neurons, and vascular cells of the cerebral cortex. J. Neurosci. *34*, 11929–11947. https://doi.org/10.1523/JNEUROSCI.1860-14.2014.

69. Zeisel, A., Hochgerner, H., Lonnerberg, P., Johnsson, A., Memic, F., van der Zwan, J., Haring, M., Braun, E., Borm, L.E., La Manno, G., et al. (2018). Molecular Architecture of the Mouse Nervous System. Cell *174*, 999–1014.e1022. https://doi.org/10.1016/j.cell.2018.06.021.

70. Kano, S.I., Choi, E.Y., Dohi, E., Agarwal, S., Chang, D.J., Wilson, A.M., Lo, B.D., Rose, I.V.L., Gonzalez, S., Imai, T., and Sawa, A. (2019). Glutathione S-transferases promote proinflammatory astrocyte-microglia communication during brain inflammation. Sci. Signal. *12*, eaar2124. https://doi.org/10.1126/scisignal.aar2124.

71. Zhang, Y., Sloan, S.A., Clarke, L.E., Caneda, C., Plaza, C.A., Blumenthal, P.D., Vogel, H., Steinberg, G.K., Edwards, M.S.B., Li, G., et al. (2016). Purification and Characterization of Progenitor and Mature Human Astrocytes Reveals Transcriptional and Functional Differences with Mouse. Neuron *89*, 37–53. https://doi.org/10.1016/j.neuron.2015.11.013.

72. Hasel, P., Rose, I.V.L., Sadick, J.S., Kim, R.D., and Liddelow, S.A. (2021). Neuroinflammatory astrocyte subtypes in the mouse brain. Nat. Neurosci. *24*, 1475–1487. https://doi.org/10.1038/s41593-021-00905-6.

73. Batiuk, M.Y., Martirosyan, A., Wahis, J., de Vin, F., Marneffe, C., Kusserow, C., Koeppen, J., Viana, J.F., Oliveira, J.F., Voet, T., et al. (2020). Identification of region-specific astrocyte subtypes at single cell resolution. Nat. Commun. *11*, 1220. https://doi.org/10.1038/s41467-019-14198-8.

74. Golovko, M.Y., Barceló-Coblijn, G., Castagnet, P.I., Austin, S., Combs, C.K., and Murphy, E.J. (2009). The role of alpha-synuclein in brain lipid metabolism: a downstream impact on brain inflammatory response. Mol. Cell. Biochem. *326*, 55–66. https://doi.org/10.1007/s11010-008-0008-y.

75. White, C.J., Ellis, J.M., and Wolfgang, M.J. (2021). The role of ethanolamine phosphate phospholyase in regulation of astrocyte lipid homeostasis. J. Biol. Chem. *297*, 100830. https://doi.org/10.1016/j.jbc.2021.100830.

76. Humphrey, J., Venkatesh, S., Hasan, R., Herb, J.T., de Paiva Lopes, K., Küçükali, F., Byrska-Bishop, M., Evani, U.S., Narzisi, G., Fagegaltier, D., et al. (2023). Integrative transcriptomic analysis of the amyotrophic lateral sclerosis spinal cord implicates glial activation and suggests new risk genes. Nat. Neurosci. *26*, 150–162. https://doi.org/10.1038/s41593-022-01205-3.

77. Li, C.Y., Yang, T.M., Ou, R.W., Wei, Q.Q., and Shang, H.F. (2021). Genome-wide genetic links between amyotrophic lateral sclerosis and autoimmune diseases. BMC Med. *19*, 27. https://doi.org/10.1186/s12916-021-01903-y.

78. Liu, W., Vetreno, R.P., and Crews, F.T. (2021). Hippocampal TNF-death receptors, caspase cell death cascades, and IL-8 in alcohol use disorder. Mol. Psychiatry *26*, 2254–2262. https://doi.org/10.1038/s41380-020-0698-4.

79. Guan, P., Zhu, D., and Wang, P. (2023). Meloxicam Inhibits Apoptosis in Neurons by Deactivating Tumor Necrosis Factor Receptor Superfamily Member 25, Leading to the Decreased Cleavage of DNA Fragmentation Factor Subunit alpha in Alzheimer's Disease. Mol. Neurobiol. *60*, 395–412. https://doi.org/10.1007/s12035-022-03091-z.

80. Turri, M., Marchi, C., Adorni, M.P., Calabresi, L., and Zimetti, F. (2022). Emerging role of HDL in brain cholesterol metabolism and neurodegenerative disorders. Biochim. Biophys. Acta. Mol. Cell Biol. Lipids *1867*, 159123. https://doi.org/10.1016/j.bbalip.2022.159123.

81. Albers, J.J., Marcovina, S.M., and Christenson, R.H. (1992). Lecithin cholesterol acyltransferase in human cerebrospinal fluid: reduced level in patients with multiple sclerosis and evidence of direct synthesis in the brain. Int. J. Clin. Lab. Res. *22*, 169–172. https://doi.org/10.1007/BF02591418.

82. Di Natale, C., Monaco, A., Pedone, C., Tessitore, A., De Mase, A., Tedeschi, G., Netti, P.A., and Abrescia, P. (2018). The level of

24-hydroxycholesteryl esters decreases in plasma of patients with Parkinson's disease. Neurosci. Lett. *672*, 108–112. https://doi.org/10.1016/j.neulet.2018.02.041.

83. Chen, Z.P., Wang, S., Zhao, X., Fang, W., Wang, Z., Ye, H., Wang, M.J., Ke, L., Huang, T., Lv, P., et al. (2023). Lipid-accumulated reactive astrocytes promote disease progression in epilepsy. Nat. Neurosci. *26*, 542–554. https://doi.org/10.1038/s41593-023-01288-6.

84. Endo, F., Kasai, A., Soto, J.S., Yu, X., Qu, Z., Hashimoto, H., Gradinaru, V., Kawaguchi, R., and Khakh, B.S. (2022). Molecular basis of astrocyte diversity and morphology across the CNS in health and disease. Science *378*, eadc9020. https://doi.org/10.1126/science.adc9020.

85. Venkataraman, A.V., Mansur, A., Rizzo, G., Bishop, C., Lewis, Y., Kocagoncu, E., Lingford-Hughes, A., Huiban, M., Passchier, J., Rowe, J.B., et al. (2022). Widespread cell stress and mitochondrial dysfunction occur in patients with early Alzheimer's disease. Sci. Transl. Med. *14*, eabk1051. https://doi.org/10.1126/scitranslmed.abk1051.

86. Shi, X., Lu, C., Corman, A., Nikish, A., Zhou, Y., Platt, R.J., Iossifov, I., Zhang, F., Pan, J.Q., and Sanjana, N.E. (2023). Heterozygous deletion of the autism-associated gene CHD8 impairs synaptic function through widespread changes in gene expression and chromatin compaction. Am. J. Hum. Genet. *110*, 1750–1768. https://doi.org/10.1016/j.ajhg.2023.09.004.

87. Burda, J.E., Bernstein, A.M., and Sofroniew, M.V. (2016). Astrocyte roles in traumatic brain injury. Exp. Neurol. *275*, 305–315.

88. Chun, H., Im, H., Kang, Y.J., Kim, Y., Shin, J.H., Won, W., Lim, J., Ju, Y., Park, Y.M., Kim, S., et al. (2020). Severe reactive astrocytes precipitate pathological hallmarks of Alzheimer's disease via H(2)O(2)(-) production. Nat. Neurosci. *23*, 1555–1566. https://doi.org/10.1038/s41593-020-00735-y.

89. Jiwaji, Z., Tiwari, S.S., Avilés-Reyes, R.X., Hooley, M., Hampton, D., Torvell, M., Johnson, D.A., McQueen, J., Baxter, P., Sabari-Sankar, K., et al. (2022). Reactive astrocytes acquire neuroprotective as well as deleterious signatures in response to Tau and Ass pathology. Nat. Commun. *13*, 135. https://doi.org/10.1038/s41467-021-27702-w.

90. Matthews, P.M. (2019). Chronic inflammation in multiple sclerosis - seeing what was always there. Nat. Rev. Neurol. *15*, 582–593. https://doi.org/10.1038/s41582-019-0240-y.

91. Ran, F.A., Cong, L., Yan, W.X., Scott, D.A., Gootenberg, J.S., Kriz, A.J., Zetsche, B., Shalem, O., Wu, X., Makarova, K.S., et al. (2015). In vivo genome editing using Staphylococcus aureus Cas9. Nature *520*, 186–191. https://doi.org/10.1038/nature14299.

92. Lee, Y., Messing, A., Su, M., and Brenner, M. (2008). GFAP promoter elements required for region-specific and astrocyte-specific expression. Glia *56*, 481–493. https://doi.org/10.1002/glia.20622.

93. Nagai, J., Rajbhandari, A.K., Gangwani, M.R., Hachisuka, A., Coppola, G., Masmanidis, S.C., Fanselow, M.S., and Khakh, B.S. (2019). Hyperactivity with Disrupted Attention by Activation of an Astrocyte Synaptogenic Cue. Cell *177*, 1280–1292.e20. https://doi.org/10.1016/j.cell.2019.03.019.

94. Yu, X., Nagai, J., Marti-Solano, M., Soto, J.S., Coppola, G., Babu, M.M., and Khakh, B.S. (2020). Context-Specific Striatal Astrocyte Molecular Responses Are Phenotypically Exploitable. Neuron *108*, 1146–1162.e10. https://doi.org/10.1016/j.neuron.2020.09.021.

95. Wheeler, M.A., Clark, I.C., Lee, H.G., Li, Z., Linnerbauer, M., Rone, J.M., Blain, M., Akl, C.F., Piester, G., Giovannoni, F., et al. (2023). Droplet-based forward genetic screening of astrocyte-microglia cross-talk. Science *379*, 1023–1030. https://doi.org/10.1126/science.abq4822.

96. van Kruining, D., Luo, Q., van Echten-Deckert, G., Mielke, M.M., Bowman, A., Ellis, S., Oliveira, T.G., and Martinez-Martinez, P. (2020). Sphingolipids as prognostic biomarkers of neurodegeneration, neuroinflammation, and psychiatric diseases and their emerging role in lipidomic investigation methods. Adv. Drug Deliv. Rev. *159*, 232–244. https://doi.org/10.1016/j.addr.2020.04.009.

97. Villegas-Llerena, C., Phillips, A., Garcia-Reitboeck, P., Hardy, J., and Pocock, J.M. (2016). Microglial genes regulating neuroinflammation in the progression of Alzheimer's disease. Curr. Opin. Neurobiol. *36*, 74–81. https://doi.org/10.1016/j.conb.2015.10.004.

98. Sienski, G., Narayan, P., Bonner, J.M., Kory, N., Boland, S., Arczewska, A.A., Ralvenius, W.T., Akay, L., Lockshin, E., He, L., et al. (2021). APOE4 disrupts intracellular lipid homeostasis in human iPSC-derived glia. Sci. Transl. Med. *13*, eaaz4564. https://doi.org/10.1126/scitranslmed.aaz4564.

99. Mi, Y., Qi, G., Vitali, F., Shang, Y., Raikes, A.C., Wang, T., Jin, Y., Brinton, R.D., Gu, H., and Yin, F. (2023). Loss of fatty acid degradation by astrocytic mitochondria triggers neuroinflammation and neurodegeneration. Nat. Metab. *5*, 445–465. https://doi.org/10.1038/s42255-023-00756-4.

100. Capece, D., Verzella, D., Flati, I., Arboretto, P., Cornice, J., and Franzoso, G. (2022). NF-kappaB: blending metabolism, immunity, and inflammation. Trends Immunol. *43*, 757–775. https://doi.org/10.1016/j.it.2022.07.004.

101. Barnard, R.A., Pomaville, M.B., and O'Roak, B.J. (2015). Mutations and Modeling of the Chromatin Remodeler CHD8 Define an Emerging Autism Etiology. Front. Neurosci. *9*, 477. https://doi.org/10.3389/fnins.2015.00477.

102. Beighley, J.S., Hudac, C.M., Arnett, A.B., Peterson, J.L., Gerdts, J., Wallace, A.S., Mefford, H.C., Hoekzema, K., Turner, T.N., O'Roak, B.J., et al. (2020). Clinical Phenotypes of Carriers of Mutations in CHD8 or Its Conserved Target Genes. Biol. Psychiatry *87*, 123–131. https://doi.org/10.1016/j.biopsych.2019.07.020.

103. Myers, S.M., Challman, T.D., Bernier, R., Bourgeron, T., Chung, W.K., Constantino, J.N., Eichler, E.E., Jacquemont, S., Miller, D.T., Mitchell, K.J., et al. (2020). Insufficient Evidence for "Autism-Specific" Genes. Am. J. Hum. Genet. *106*, 587–595. https://doi.org/10.1016/j.ajhg.2020.04.004.

104. Vargas, D.L., Nascimbene, C., Krishnan, C., Zimmerman, A.W., and Pardo, C.A. (2005). Neuroglial activation and neuroinflammation in the brain of patients with autism. Ann. Neurol. *57*, 67–81. https://doi.org/10.1002/ana.20315.

105. Krakowiak, P., Goines, P.E., Tancredi, D.J., Ashwood, P., Hansen, R.L., Hertz-Picciotto, I., and Van de Water, J. (2017). Neonatal Cytokine Profiles Associated With Autism Spectrum Disorder. Biol. Psychiatry *81*, 442–451. https://doi.org/10.1016/j.biopsych.2015.08.007.

106. Zerbo, O., Yoshida, C., Grether, J.K., Van de Water, J., Ashwood, P., Delorenze, G.N., Hansen, R.L., Kharrazi, M., and Croen, L.A. (2014). Neonatal cytokines and chemokines and risk of Autism Spectrum Disorder: the Early Markers for Autism (EMA) study: a case-control study. J. Neuroinflammation *11*, 113. https://doi.org/10.1186/1742-2094-11-113.

107. Craft, J.M., Watterson, D.M., and Van Eldik, L.J. (2005). Neuroinflammation: a potential therapeutic target. Expert Opin. Ther. Targets *9*, 887–900. https://doi.org/10.1517/14728222.9.5.887.

108. Liu, P., Wang, Y., Sun, Y., and Peng, G. (2022). Neuroinflammation as a Potential Therapeutic Target in Alzheimer's Disease. Clin. Interv. Aging *17*, 665–674. https://doi.org/10.2147/CIA.S357558.

109. Wang, Q., Liu, Y., and Zhou, J. (2015). Neuroinflammation in Parkinson's disease and its potential as therapeutic target. Transl. Neurodegener. *4*, 19. https://doi.org/10.1186/s40035-015-0042-0.

110. Sofroniew, M.V. (2015). Astrocyte barriers to neurotoxic inflammation. Nat. Rev. Neurosci. *16*, 249–263.

111. Colonna, M., and Brioschi, S. (2020). Neuroinflammation and neurodegeneration in human brain at single-cell resolution. Nat. Rev. Immunol. *20*, 81–82. https://doi.org/10.1038/s41577-019-0262-0.

112. Hata, M., Andriessen, E.M.M.A., Hata, M., Diaz-Marin, R., Fournier, F., Crespo-Garcia, S., Blot, G., Juneau, R., Pilon, F., Dejda, A., et al. (2023). Past history of obesity triggers persistent epigenetic changes in

innate immunity and exacerbates neuroinflammation. Science *379*, 45–62. https://doi.org/10.1126/science.abj8894.

113. Hamel, R., Peruzzotti-Jametti, L., Ridley, K., Testa, V., Yu, B., Rowitch, D., Marioni, J.C., and Pluchino, S. (2023). Time-resolved single-cell RNA-seq profiling identifies a novel Fabp5(+) subpopulation of inflammatory myeloid cells with delayed cytotoxic profile in chronic spinal cord injury. Heliyon *9*, e18339. https://doi.org/10.1016/j.heliyon.2023.e18339.

114. Yu, X., Nagai, J., and Khakh, B.S. (2020). Improved tools to study astrocytes. Nat. Rev. Neurosci. *21*, 121–138. https://doi.org/10.1038/s41583-020-0264-8.

115. Wei, H., Wu, X., You, Y., Duran, R.C.D., Zheng, Y., Narayanan, K.L., Hai, B., Li, X., Tallapragada, N., Prajapati, T.J., et al. (2021). Systematic analysis of purified astrocytes after SCI unveils Zeb2os function during astrogliosis. Cell Rep. *34*, 108721. https://doi.org/10.1016/j.celrep.2021.108721.

116. Guttenplan, K.A., Stafford, B.K., El-Danaf, R.N., Adler, D.I., Münch, A.E., Weigel, M.K., Huberman, A.D., and Liddelow, S.A. (2020). Neurotoxic Reactive Astrocytes Drive Neuronal Death after Retinal Injury. Cell Rep. *31*, 107776. https://doi.org/10.1016/j.celrep.2020.107776.

117. Soto, J.S., Jami-Alahmadi, Y., Chacon, J., Moye, S.L., Diaz-Castro, B., Wohlschlegel, J.A., and Khakh, B.S. (2023). Astrocyte-neuron subproteomes and obsessive-compulsive disorder mechanisms. Nature *616*, 764–773. https://doi.org/10.1038/s41586-023-05927-7.

118. Sorensen, A.T., Cooper, Y.A., Baratta, M.V., Weng, F.J., Zhang, Y., Ramamoorthi, K., Fropf, R., LaVerriere, E., Xue, J., Young, A., et al. (2016). A robust activity marking system for exploring active neuronal ensembles. Elife *5*. https://doi.org/10.7554/eLife.13918.

119. Sun, X., Bernstein, M.J., Meng, M., Rao, S., Sørensen, A.T., Yao, L., Zhang, X., Anikeeva, P.O., and Lin, Y. (2020). Functionally Distinct Neuronal Ensembles within the Memory Engram. Cell *181*, 410–423.e17. https://doi.org/10.1016/j.cell.2020.02.055.

120. Leger, M., Quiedeville, A., Bouet, V., Haelewyn, B., Boulouard, M., Schumann-Bard, P., and Freret, T. (2013). Object recognition test in mice. Nat. Protoc. *8*, 2531–2537. https://doi.org/10.1038/nprot.2013.155.

121. Can, A., Dao, D.T., Terrillion, C.E., Piantadosi, S.C., Bhat, S., and Gould, T.D. (2012). The tail suspension test. J. Vis. Exp., 3769. https://doi.org/10.3791/3769.

122. Amar, M., Pramod, A.B., Yu, N.K., Herrera, V.M., Qiu, L.R., Moran-Losada, P., Zhang, P., Trujillo, C.A., Ellegood, J., Urresti, J., et al. (2021). Autism-linked Cullin3 germline haploinsufficiency impacts cytoskeletal dynamics and cortical neurogenesis through RhoA signaling. Mol. Psychiatry *26*, 3586–3613. https://doi.org/10.1038/s41380-021-01052-x.

123. Gandal, M.J., Zhang, P., Hadjimichael, E., Walker, R.L., Chen, C., Liu, S., Won, H., van Bakel, H., Varghese, M., Wang, Y., et al. (2018). Transcriptome-wide isoform-level dysregulation in ASD, schizophrenia, and bipolar disorder. Science *362*, eaat8127. https://doi.org/10.1126/science.aat8127.

124. Martin, M. (2011). Cutadapt removes adapter sequences from high-throughput sequencing reads. EMBnet. j. *17*, 10. https://doi.org/10.14806/ej.17.1.200.

125. Dobin, A., Davis, C.A., Schlesinger, F., Drenkow, J., Zaleski, C., Jha, S., Batut, P., Chaisson, M., and Gingeras, T.R. (2013). STAR: ultrafast universal RNA-seq aligner. Bioinformatics *29*, 15–21. https://doi.org/10.1093/bioinformatics/bts635.

126. Ewels, P., Magnusson, M., Lundin, S., and Käller, M. (2016). MultiQC: summarize analysis results for multiple tools and samples in a single report. Bioinformatics *32*, 3047–3048. https://doi.org/10.1093/bioinformatics/btw354.

127. Li, B., and Dewey, C.N. (2011). RSEM: accurate transcript quantification from RNA-Seq data with or without a reference genome. BMC Bioinf. *12*, 323. https://doi.org/10.1186/1471-2105-12-323.

128. Robinson, M.D., McCarthy, D.J., and Smyth, G.K. (2010). edgeR: a Bioconductor package for differential expression analysis of digital gene expression data. Bioinformatics *26*, 139–140. https://doi.org/10.1093/bioinformatics/btp616.

129. Zhou, Y., Zhou, B., Pache, L., Chang, M., Khodabakhshi, A.H., Tanaseichuk, O., Benner, C., and Chanda, S.K. (2019). Metascape provides a biologist-oriented resource for the analysis of systems-level datasets. Nat. Commun. *10*, 1523. https://doi.org/10.1038/s41467-019-09234-6.

130. Reimand, J., Isserlin, R., Voisin, V., Kucera, M., Tannus-Lopes, C., Rostamianfar, A., Wadi, L., Meyer, M., Wong, J., Xu, C., et al. (2019). Pathway enrichment analysis and visualization of omics data using g:Profiler, GSEA, Cytoscape and EnrichmentMap. Nat. Protoc. *14*, 482–517. https://doi.org/10.1038/s41596-018-0103-9.

131. Yu, G., Wang, L.G., Han, Y., and He, Q.Y. (2012). clusterProfiler: an R package for comparing biological themes among gene clusters. OMICS *16*, 284–287. https://doi.org/10.1089/omi.2011.0118.

132. Bolger, A.M., Lohse, M., and Usadel, B. (2014). Trimmomatic: a flexible trimmer for Illumina sequence data. Bioinformatics *30*, 2114–2120. https://doi.org/10.1093/bioinformatics/btu170.

133. Liao, Y., Smyth, G.K., and Shi, W. (2014). featureCounts: an efficient general purpose program for assigning sequence reads to genomic features. Bioinformatics *30*, 923–930. https://doi.org/10.1093/bioinformatics/btt656.

134. Love, M.I., Huber, W., and Anders, S. (2014). Moderated estimation of fold change and dispersion for RNA-seq data with DESeq2. Genome Biol. *15*, 550. https://doi.org/10.1186/s13059-014-0550-8.

135. Langmead, B., and Salzberg, S.L. (2012). Fast gapped-read alignment with Bowtie 2. Nat. Methods *9*, 357–359. https://doi.org/10.1038/nmeth.1923.

136. Zhang, Y., Liu, T., Meyer, C.A., Eeckhoute, J., Johnson, D.S., Bernstein, B.E., Nusbaum, C., Myers, R.M., Brown, M., Li, W., and Liu, X.S. (2008). Model-based analysis of ChIP-Seq (MACS). Genome Biol. *9*, R137. https://doi.org/10.1186/gb-2008-9-9-r137.

STAR★METHODS

KEY RESOURCES TABLE

REAGENT or RESOURCE	SOURCE	IDENTIFIER
Antibodies		
CHD8 Rabbit polyclonal 1 to 500	Abcam	ab84527
CHD8 Rabbit polyclonal 1 to 1000	Novus Biologicals	NB 100-60418
GFAP Guinea pig polyclonal antiserum 1 to 1000	Synaptic Systems	173 004
Iba1 Chicken polyclonal 1 to 1000	Synaptic Systems	234 006
Iba1 Rabbit Monoclonal 1 to 1000	Abcam	ab178846
BrdU Mouse Monoclonal 1 to 200	Sigma-Aldrich	MAB4072
Ki67 Rabbit Monoclonal 1 to 500	Invitrogen	MA5-14520
tdTomato Rat Monoclonal 1 to 500	Kerafast	EST203
LCAT Rabbit polyclonal 1 to 200 for IHC, 1 to 500 for WB	Invitrogen	PA5-22965
DR3/TNFRSF25 Mouse Monoclonal 1 to 200 for IHC,1 to 500 for WB	R&D Systems	MAB943
SOX9 Goat antiserum 1 to 200	R&D Systems	AF3075
HA tag Rat IgG1 1 to 200	Roche	11867431001
goat-*anti*-mouse IRDye680	Li-COR Biosciences	926–68070
donkey-*anti*-rabbit IRDye 800CW	Li-COR Biosciences	926–32213
Bacterial and virus strains		
pAAV2/5	Addgene	Addgene # 104964
pAdDeltaF6 helper	Addgene	Addgene # 112867
pAAV-U6-scramble-GfaABC$_1$D-SaCas9-HA vector	This paper	N/A
pAAV-U6-*Rosa26*-GfaABC$_1$D-SaCas9-HA vector	This paper	N/A
pAAV-U6-*Chd8*-GfaABC$_1$D-SaCas9-HA vector	This paper	N/A
Chemicals, peptides, and recombinant proteins		
Tamoxifen	Sigma	T5648
OptiPrep Density Gradient	Sigma	D1556
DAPI	Sigma	D9542
Antifade mounting medium	Vector Laboratories	VECTH1000
BrdU	Sigma	B5002
Lipopolysaccharide	Sigma	L2880
Cas9 protein	NEB	M0646T
Critical commercial assays		
RNA synthesis kit	NEB	E2040S
LA-PCR	Takara	RR002A
RNeasy mini kit	QIAGEN	74104
iScript cDNA Synthesis Kit	Bio-Rad	1725035
iQ SYBR Green Super mix kit	Bio-Rad	1708882
TruSeq ribodepleted mRNA stranded for library preparation	Illumina	20020594
ATAC-Seq Kit	Active Motif	53150
Adult Brain Dissociation Kit, mouse and rat	Miltenyi Biotec	130-107-677
Anti-CD11b Magnetic Microbeads kit for microglia	Miltenyi Biotec	130–093-634
Anti-ACSA-2 MicroBead Kit for astrocyte	Miltenyi Biotec	130-097-678
Deposited data		
Tissue Bulk RNA-seq data	NCBI - Gene Expression Omnibus	GEO accession number: GSE271650
Microglia Bulk RNA-seq data	NCBI - Gene Expression Omnibus	GEO accession number: GSE271651
Astrocyte ATAC-seq data	NCBI - Gene Expression Omnibus	GEO accession number: GSE271652

(*Continued on next page*)

Continued

REAGENT or RESOURCE	SOURCE	IDENTIFIER
Experimental models: Organisms/strains		
Chd8$^{fx/fx}$ mouse line	This paper	N/A
CAGGS-CreER mouse line	Feng lab[34]	N/A
Aldh1l1-CreER^{T2} mouse line	Jackson	#029655
Tmem119-CreER^{T2} mouse line	Jackson	#031820
Oligonucleotides		
See Table S2 for a detailed list of primers used in this study	IDT	
Software and algorithms		
ZEN 3.6 blue edition	Zeiss	SCR_013672
Fiji	NIH	RRID:SCR_002285
Cellpose	https://github.com/MouseLand/cellpose	RRID:SCR_021716
MATLAB R2022a	MathWorks	RRID:SCR_001622
3DMorph	https://github.com/ElisaYork/3DMorph	
GraphPad Prism 9	GraphPad Software	RRID:SCR_002798
HVS Image 2020	HVS Image, UK	

RESOURCE AVAILABILITY

Lead contact

Further information and requests for resources and reagents should be directed to the lead contact, Yang Zhou (yang.zhou7@mcgill.ca).

Materials availability

All unique/stable reagents generated in this study are available from the lead contact, Yang Zhou (yang.zhou7@mcgill.ca) with a completed Materials Transfer Agreement.

Data and code availability

- RNA-seq and ATAC-seq data have been deposited at GEO and are publicly available as of the date of publication. Accession numbers are listed in the key resources table. Original western blot images and microscopy data reported in this paper will be shared by the lead contact upon request.
- This paper does not report original code.
- Any additional information required to reanalyze the data reported in this work is available from the lead contact upon request

EXPERIMENTAL MODEL AND STUDY PARTICIPANT DETAILS

All animal procedures have been approved by the Animal Care Committee at the Montreal Neurological Institute of McGill University, in accordance with the guidelines of the Canadian Council on Animal Care. Mice were co-housed with littermates (2–5 per cage) in a temperature-controlled (22–24°C) and humidity-controlled (40–60%) environment on a 12-h light/dark cycle with *ad libitum* food and water. Male and female mice, age-matched and from the same litter when possible, were assigned to experimental conditions. The exact number of animals (n) for each experiment is reported in the legend of each figure. *CAGGS*-CreER (Feng lab at MIT),[33] *Aldh1l1*-CreERT2 (Jackson strain # 029655),[43] and *Tmem119*-CreERT2[51] (Jackson strain # 031820) mice were maintained in a C57BL/6J background.

The *Chd8*$^{fx/fx}$ targeting vector was designed by flanking exon 4 with two *loxP* cassettes through homologous recombination facilitated by CRISPR/Cas9-induced double-strand break. The guide RNA (5′- ccgaggggatgaggatattt-3′) was functionally tested for editing first, then prepared using an *in vitro* RNA synthesis kit (NEB, E2040S). The gRNA was co-injected with Cas9 protein (NEB, M0646T) and HR vector into the cytoplasm of C57BL/6J-derived fertilized eggs with well-identified pronuclei. Correct locus insertion of the targeting construct into the genomic DNA of newborn mice was determined by LA-PCR (Takara, RR002A) followed by Sanger sequencing of the amplicon. Confirmed flox mice were back-crossed with C57BL/6J for more than six generations and maintained in the congenic C57BL/6J background. Subsequent mouse genotyping was determined by standard PCR (Bioline, BIO-21040) of mouse tail or ear DNA using two primers: (Forward: 5′-gtgaggttatattcgtgtgagc-3′) and (Reverse: 5′-aaggtggaaaaggctatacagc-3′). These primers produce a band of 355 bp for the WT allele and a band of 389 bp for the floxed allele.

For the adult *Chd8* Global cKO experiments, the *Chd8*$^{fx/fx}$ mice were crossed with *CAGGS*-CreER$^{+/-}$ animals.[33] For the astrocyte-specific *Chd8* ablation experiments, the *Chd8*$^{fx/fx}$ mice were crossed with *Aldh1l1*-CreERT2$^{+/-}$ [43]. For the microglia-specific *Chd8*

ablation experiments, the *Chd8*$^{fx/fx}$ mice were crossed with *Tmem1119*-CreERT2$^{+/-}$ [51]. To produce adequate animals for all necessary experiments, breeding strategy was optimized to heterozygotes crossed with heterozygotes and homozygotes crossed with homozygotes for all conditions (*Chd8*$^{fx/fx}$: *CAGGS*-CreER$^{+/-}$ bred with *Chd8*$^{fx/fx}$: *CAGGS*-CreER$^{-/-}$; *Chd8*$^{fx/fx}$: *Aldh1l1*-CreERT2$^{+/-}$ bred with *Chd8*$^{fx/fx}$: *Aldh1l1*-CreERT2$^{-/-}$: *Aldh1l1*-CreERT2$^{-/-}$; *Chd8*$^{fx/fx}$: *Tmem119*-CreERT2$^{+/-}$ bred with *Chd8*$^{fx/fx}$: *Tmem119*-CreERT2$^{-/-}$). Age- and sex-matched littermates were randomly assigned to different treatment and experimental groups. No computerized randomization program was used.

METHOD DETAILS

Tamoxifen preparation and feeding

Tamoxifen (Sigma, T5648) was dissolved in corn oil at a concentration of 20 mg/mL by vortexing. Freshly prepared tamoxifen was protected from light by aluminum foil and kept at 4°C for 2–3 days. Disposable animal feeding needles (Fisher Scientific, 01-208-87) were used for oral gavage to adult mice (more than 2 months old). To avoid the excessive toxicity of tamoxifen, the following dosages were optimized and used for adult animals: mice at 22–25 g body weight were fed 6 mg/day; mice at 26–29 g body weight were fed 7 mg/day; mice at 30–35 g body weight were fed 8 mg/day. The adult mice were fed for 5 consecutive days followed by 4 weeks of rest before being subjected to experimental procedures. That time frame was chosen so that *Chd8* was no longer detectable in brain cells of interest in cKO animals, as determined by IHC.

Viral vectors, *in vivo* gene editing, and surgical procedures on mice

The packaging plasmid expressing Rep/Cap genes for the production of serotype 5 (Plasmid #104964) and the pAdDeltaF6 helper (Plasmid #112867) were both obtained from the Addgene. To identify the effective gRNA that allows for robust *in vivo* editing (knock out) of the *Chd8* gene, multiple gRNAs were designed, synthesized, and tested in primary mouse fibroblast through quantitative analysis of *Chd8* mRNA. The effective gRNA (5′- GGATTGTGGCAGAGGCCATTGC-3′) was utilized for the AAV package. The two AAV vectors: U6-Scramble-gRNA-GfaABC$_1$D-SaCas9 and AAV5-U6-*Chd8*-gRNA-GfaABC$_1$D-SaCas9 were constructed through standard cloning. AAVs were generated in HEK293T cells and purified using a purification protocol through OptiPrep Density Gradient.[118,119]

Animals were 3–6 months old at the time of surgery. Mice were anesthetized with 2% isoflurane with an O_2 flow rate of 2 L/min and head-fixed in a stereotactic frame (David Kopf). Eyes were lubricated with an ophthalmic ointment, and body temperature was maintained at 37°C with a warm water recirculator (Stryker). The fur was shaved, and the incision site was sterilized before beginning surgical procedures. Carprofen was provided for analgesia. For the ‘‘stab-wound’’ injury procedure, the lambda and bregma were aligned to the same plane. The location of the injury was determined to be performed at coordinates ML = 1.5, AP = −1.95, and DV = 2.4. To access the brain, an entry point with a diameter of less than 2 mm was created through the skull using a fine micromotor drill (Stoelting, 51449). For consistency in injury size, a 5 μL Microliter Syringe (Hamilton, Model 75 N #89700) was mounted on the stereotactic frame via a microinjector (Harvard apparatus device, 70–4507) and used for AAV injection or introducing standardized ‘‘stab-wound injury’’ to the mouse brains. After reaching the desired dorsoventral point, the needle was kept in place for 5 min before being subtracted. The incision was then sutured, and mice were left to recover fully over a warm water recirculator. Postsurgical care was provided with daily subcutaneous injections of carprofen once per day for 3 consecutive days post-surgery. For AAV injections and simultaneous stab-wound injury, we utilized the same procedure and coordinates (ML = 1.5, AP = −1.95, and DV = 2.4) as for the stab-wound injury. The same type of Hamilton syringe was used for the AAV injections. Briefly, ∼1 μL of mineral oil was drawn into the syringe to negate negative space. Then 4 μL of viruses were loaded into the syringe which was mounted to the micro injector. After reaching the desired dorsoventral point (DV = 2.4), 1.5 μL of AAVs were injected at the rate of 0.1 μL/min. The needle was then left in the position for 5 min. Subsequently, the needle was withdrawn slightly so that it would reach a new DV position at DV = 1.9, another 1 μL (0.1 μL/min) of the virus was injected, and again the needle was maintained at the position for 5 min. Finally, the needle was withdrawn slightly so that it would reach a new DV position at DV = 1.4, and another 1 μL (0.1 μL/min) of the virus was injected again with the needle maintained at the position for a final 5 min. The needle was then retracted completely, and the incision was sutured. Mice were left to recover fully over a warm water recirculator. Postsurgical care was provided with daily subcutaneous injections of carprofen for 3 days after surgery.

Immunohistochemistry and imaging of brain slices

At the experiment’s endpoint, mice were transcardially perfused with PBS followed by 4% paraformaldehyde, and brains were kept in 4% paraformaldehyde at 4°C overnight. The next day, brains were switched into a PBS solution and sectioned into 50 μm slices using a Leica VT1000s vibrating blade microtome. Floating slices were kept in a PBS solution until further processing for IHC experiments, using the appropriate protocol. For CHD8, TNFRSF25, and LCAT IHC experiments, slices were first subjected to antigen retrieval in Sodium Citrate buffer (10 mM Sodium Citrate, 0.05% Tween 20, pH 6.0). Brain slices were heated to just below boiling (95°C) using a heating block for 15 min and then left to cool down to room temperature. Slices were then washed with PBS solution and permeabilized with 1.2% Triton X- for 15 min. After washing again 3 times in PBS, slices were blocked in blocking solution for 1 h (0.2% Triton X-, 2% Bovine Serum Albumin, 5% Normal Goat Serum, diluted in PBS). Slices were then incubated overnight in the appropriate concentration of primary antibodies diluted in blocking solution. For BrdU staining, slices were subjected to antigen retrieval in an

HCl solution. Free-floating slices were added to 2N HCl solution at 37°C for 20 min, and then they were added to 0.1 M Sodium Borate solution for 10 min, followed by 3 washes for 10 min in ice-cold PBS. Before adding primary antibodies, they were blocked for 2 h in a blocking solution (3% Normal Goat Serum, 0.3% Triton X- in PBS). After overnight incubation with primary antibodies at 4°C, slices from all preparations were washed 3 times in PBS for 20 min each and then were incubated overnight in the appropriate secondary antibodies at 4°C. Slices were then washed 3 times with PBS for 20 min and subsequently incubated with DAPI (Sigma, D9542) at the concentration of 1 μL/mL diluted in PBS for 10 min. After a final washing step of 20 min with PBS, slices were mounted onto glass slides and covered with coverslips in antifade mounting medium (Vector Laboratories, VECTH1000) and sealed with nail polish. After cure overnight, slices were stored short-term at 4°C until imaging. Confocal imaging was performed using an LSM 700 laser scanning confocal microscope. For images where higher magnifications were required, the 63× oil objective was used, and z-stacks were acquired. Then maximum intensity projections were prepared using the LSM software (ZEN 2011, ZEN 3.6 blue edition). For images where signal bleed-through was observed, the spectral unmixing algorithm was utilized from the ZEN software.

Reactive gliosis quantification for the "stab-wound" injury method

Ten days after surgery, mice were transcardially perfused with PBS followed by 4% PFA and brain slices at the thickness of 50 μm were sectioned consecutively. Of the 20 slices most proximal to the injury site, 16 slices were randomly picked for IHC. Of those, 4 slices from each animal (one slice per 4 consecutive slices, picked randomly) were assigned as negative controls and were stained only with the appropriate secondary antibodies in parallel with the rest of the slices. The remaining 12 slices were stained with GFAP and Iba1 antibodies, then mounted onto glass slides with 6 slices on each slide. For imaging, collages of the whole slide were acquired using a Nikon Eclipse Ti Epi-fluorescence microscope with a Plan-Fluor 10x/0.3 objective and a Zyla sCMOS camera. For quantification of the GFAP and Iba1 response, the area occupied by the fluorescent signal was quantified.[41] Specifically, a standard region of interest engulfing the whole hippocampus and the maximal response range was set and used for all animals (see also Figure S3A). The contralateral brain region corresponding to the ipsilateral injury area was first analyzed, with the region of interest subjected to color thresholding via the ImageJ function. To determine the appropriate threshold for each brain slice, the "Moments" function was used in the contralateral site's ROI for GFAP and Iba1 signals. The thresholded area was then quantified. For the ipsilateral side, the same threshold value was used to determine the area of the respective signals (see also Figures S3B–S3E). The areas were then divided by the total area of the ROI, to be calculated as the fraction of the ROI occupied by the signal. The values calculated for the ipsilateral and contralateral sites were then used for statistical analysis. To quantify the cell numbers in the same regions of interest, we use the Python code Cellpose.[48] Specifically, the same regions of interest utilized for area quantification were used and the parameters were set to optimally incorporate most cells in each region of interest (model: cyto fluorescence). Values calculated for the ipsilateral and contralateral sites were then used for statistical analysis.

Assay of astrocyte proliferation *in vivo*

For detecting proliferating astrocytes after mechanical injury, BrdU (Sigma: B5002) incorporation assay and Ki67 staining were used. Mice were subjected to stab wound injury first. Three days after injury, BrdU was intraperitoneally injected into the animals daily at a dose of 50 mg/kg (diluted in endotoxin-free physiological saline). Seven days after the injury, animals were transcardially perfused with PBS followed by 4% PFA and brains were sliced for staining. Six slices most proximal to the injury site were picked and counterstained with BrdU, Ki67, and tdTomato antibodies. For quantification, confocal images using the 10x objective were taken to cover the whole injury area and stitched together using the ImageJ software. Stitched images were used for BrdU and Ki67 quantification as follows. Using the image calculator function of ImageJ, images containing the channels Ki67 & DAPI, BrdU & DAPI, Ki67 & DAPI & tdTomato, BrdU & DAPI & tdTomato, were generated. Then the resulting positive nuclei were displayed and counted manually.

Sholl analysis and characterization of cell morphology

For astrocyte morphology characterization, the slices with the epicenter of the "stab-wound" injury were chosen and z-stacks of an area within 300 μm of the needle track were taken, utilizing the 63x oil objective. For microglia morphology characterization, z-stacks images also taken with the 63x objective were utilized. For cell morphology quantification, we used the MATLAB code (MATLAB R2022a) 3DMorph.[55] Briefly, the parameters for cell segmentation were optimized for each image. From the outputted cells, the ones where segmentation was not successful were filtered, and the top-scored cells from each mouse were utilized for further statistical analysis. Cell parameters such as cell territory volume, cell volume, ramification index, number of branch points, and average and maximum branch lengths were calculated by the software and used for statistical analysis. Cell ramification index is calculated by territorial volume divided by cell volume. This is a measure of how ramified or ameboid the cells are. Skeletonized images of the cells were generated by the software and were subsequently processed in ImageJ and the Neuroanatomy plugin for the Sholl analysis. As the generated skeletonized images by the software were scaled in arbitrary units, the sizes were changed to correspond to the dimensions of the images in ImageJ (For example, 1 a.u. = 0.2 μm). Maximum and Average branch lengths were also expressed in arbitrary units and they were changed accordingly. For the statistical analysis of the Sholl analysis data, the mixed effects model was used to determine the range of distances from the soma with statistically significant differences between genotypes.

LPS administration

Lipopolysaccharide (Sigma, L2880) was injected intraperitoneally into mice between 4 and 6 months old at a dose of 5 mg/kg, diluted in endotoxin-free physiological saline (Teligent). For temperature measurements, a Far Infrared Warming Pad Controller and a RightTemp rectal probe sensor (Kent Scientific) were used, and three data points were collected the day before the start of the experiment and one immediately before injection, to establish a baseline. Temperature was collected every 90 min from 10 a.m. to 10 p.m. each day for the first 48 h after injection. Seventy-two hours post LPS injection, brain tissues from mice were directly harvested and dissected and were kept at −80°C for mRNA and protein assays. For these collected tissues, cortical tissue from one hemisphere was used for RNA isolation, and tissue from the other hemisphere was processed for protein quantification via western blotting. For immunohistochemistry and imaging, another set of saline and LPS-injected mice were utilized. Mice were transcardially perfused with PSB followed by 4% paraformaldehyde and brains were kept in 4% paraformaldehyde at 4°C overnight. The next day, brains were switched into a PBS solution and sectioned into 50 μm slices using a Leica VT1000s vibrating blade microtome.

Behavioral assessments

Open field test

One day before LPS administration, mice were subjected to the open field test to habituate. Briefly, mice were placed in the center of an empty testing area (40 × 40 cm; 30cm height, Maze Engineers) and allowed to move freely for 10 min. The session was recorded and quantified using the HVS Image software (HVS Image 2020; HVS Image Software Ltd.). The following day, mice were injected with LPS (5 mg/kg) or an equivalent volume of physiological saline. 24 h after the injections, mice were placed again in the open field chamber for exploration for 10 min.

Novel object recognition test

The novel object recognition (NOR) test was modified based on Leger et al., 2013.[120] Tests were performed 24 h after LPS or Saline injections. A 10-min open field test was utilized as habituation. Immediately after, two identical objects were placed in the arena, and the mouse was placed on the opposite third. Mice were allowed to explore the arena for 10 min before being returned to their home cage. After 3 h, mice were placed back in the arena with one of the identical objects replaced by a novel object. The time spent exploring each of the objects and the number of interactions with each of the objects were recorded. Time spent exploring was the amount of time the mouse spent within a 2 cm radius of each object. Number of interactions was recorded by counting the number of times the mouse directed its nose toward the object while inside the 2 cm border surrounding the object. Quantification of NOR was performed by a trained observer blinded to the genotype and treatment of mice.

Tail suspension test

After the testing phase of the novel object recognition test, mice were subjected to the tail suspension test.[121] Briefly, a 17cm tape was attached to the end of the mouse tail and the other end to a metal bar so that the nose of the mouse would be approximately 20–25 cm from the bottom. As the C57/B6 mouse strain has been known to have a strong tail climbing behavior, the mouse tail was fitted through a plastic cylinder to discourage this climbing behavior. The test was conducted for 6 min, with extra time recorded to account for any time the mouse spent climbing its tail, as any time spent tail climbing was completely removed from the final analysis. The amount of time spent immobile was analyzed by a trained observer blinded to the genotype and treatment of mice.

Western blotting and protein quantification

Sonicated tissue samples were mixed with 200–300 μL 2x Laemmli sample buffer (Bio-Rad). Subsequently, the mixture was boiled for 10 min at 95°C. Sample volumes corresponding to 20 μg protein per lane were loaded onto 4–15% gradient Mini-PROTEAN TGX gels (Bio-Rad) and run for 4 h at 60–70 V. The proteins were then transferred onto nitrocellulose membranes (Amersham, GE10600004) using a tank blot system (Mini Trans-Blot Cell, Bio-Rad) for 120 min at 400 mA submerged in an ice bath. The membranes were blocked for 1 h with 5% non-fat milk dissolved in TBS, at room temperature. Subsequently, the membranes were incubated with primary antibodies diluted in blocking buffer plus 0.05% Tween 20, overnight at 4°C. Following primary antibody incubation, the membranes were washed three times for 5 min per wash using TBST buffer (0.05% Tween 20). Then, the secondary antibodies, goat-*anti*-mouse IRDye680 (Li-COR Biosciences), donkey-*anti*-rabbit IRDye 800CW (Li-COR Biosciences), diluted in 1:1 TBST (0.05% Tween 20): Odyssey Blocking Buffer (Li-COR Biosciences) were incubated with the membrane overnight at 4°C. Following three rounds of washing with TBST, the membranes were scanned using an Odyssey CLx infrared imaging system (Li-COR Biosciences). Specific bands were then quantified with the contrast-independent, automatic background subtraction rectangular ROI tool of the built-in Software Image Studio 3.1 (Li-COR Biosciences) and normalized to GAPDH loading control for each lane and each blot. The values obtained for the target group were then normalized to the expression level in the control group.

RNA isolation and real-time Q-PCR assay

Total RNA was extracted from dissected cortices of LPS-treated animals from both genotypes, using the RNeasy mini kit (QIAGEN, 74104) following the standard user manual. An equivalent amount of total mRNA was reversely transcripted to cDNAs with iScript cDNA Synthesis Kit (Bio-Rad, 1725035). Quantitative real-time PCR (qPCR) was carried out using the CFX Opus 96 real-time PCR detection system (Bio-Rad) with the iQ SYBR Green Super mix kit (Bio-Rad, 1708882) following the guidelines of the manufacturer's manual.

Bulk RNA sequencing and analytic pipeline

Total RNA was isolated from mouse brain tissues and was processed using TruSeq ribodepleted mRNA stranded for library preparation (Illumina, 20020594). Paired-end RNA sequencing (2 × 100 bp) was performed on an Illumina NovaSeq6000 sequencer to an average depth of about 40 million reads per sample. The raw sequencing files from all 18 mouse brain samples were processed through a unified paired-end RNA sequencing analysis pipeline, which is based on previous studies.[122,123] Adapter sequences, low base call quality (Phred score <30), and reads with fewer than 5 bases, were trimmed from all FASTQ files using Cutadapt (v3.5).[124] FastQC (Babraham Bioinformatics) was used before and after trimming to assess quality control. STAR[125] aligner was used to align trimmed sequences to the mouse reference genome (GRCm39) with gene annotations from mouse Gencode (vM28). MultiQC (v1.12)[126] was used to assess the quality of alignment. All aligned samples showed more than 80% uniquely mapped reads. Gene count quantifications were analyzed using RSEM (RNA-Seq by Expectation Maximization; v.1.3.1).[127]

Differential expressed genes (DEGs) analysis

Expected gene count quantifications from RSEM analysis were imported into R for differential gene analysis using edgeR (v.3.30.3).[128] Genes with median log2 counts per million $\geq$ 1 were considered expressed, resulting in 13,861 genes as downstream processing across all samples. Differential gene analysis was performed using the negative binomial generalized linear model approach of edgeR and using genotype and treatment as covariates. Significant genes are defined as genes with a false discovery rate (FDR) < 0.05, with Benjimini-Hochberg multiple comparison correction.

Enrichment analysis

Functional pathway analysis was performed using Metascape,[129] gProfiler,[130] and ClusterProfiler.[131] Cell-type marker enrichment was calculated using the hypergeometric test with Benjamini-Hochberg multiple comparison correction.

Isolation of astrocytes and microglia from adult mouse brains

2-3 month old mice were transcardially perfused under deep anesthesia with 1 X PBS, and brain was removed, dissected, and rinsed. Cortical and hippocampal tissue were isolated and dissected with the gentleMACS Octo Dissociator (Miltenyi Biotec) according to the manufacturer's instructions. For adult mouse brains, the Adult Brain Dissociation Kit (Miltenyi Biotec), was used. After myelin removal, total cells were counted to proceed to the MACS step. Cell suspensions containing approximately 1x10E^6 cells were labeled with superparamagnetic MicroBeads coupled to antibodies specific for the astrocyte marker ACSA-2 (Anti-ACSA-2 MicroBead Kit, 130-097-678, Miltenyi Biotec). Before antibody labeling, nonspecific binding to the Fc receptor was blocked using the FcR Blocking Reagent, mouse (Miltenyi Biotec). Cells were suspended in PBS with 0.5% BSA and the cell suspension was loaded onto an MS Column (Miltenyi Biotec), which was placed in the magnetic field of a MiniMACS Separator (Miltenyi Biotec). The magnetically labeled ACSA-2-positive cells were retained within the column and eluted as the positively selected cell fraction after removing the column from the magnet. The negative cell fraction was then used and incubated with Anti-CD11b Magnetic Microbeads (130–093-634, Miltenyi Biotec). Cells were suspended in PBS with 0.5% BSA and the cell suspension was loaded onto an MS Column (Miltenyi Biotec), which was placed in the magnetic field of a MiniMACS Separator (Miltenyi Biotec). The magnetically labeled CD11b-positive cells were retained within the column and eluted as the positively selected cell fraction after removing the column from the magnet.

RNA-seq library preparation and analysis for microglia-enriched samples

Microglia-enriched cells were collected and total RNA was isolated the Trizol (Cat#15596026; Thermo Fisher Scientific) method as provided in the manual from supplier. For library preparation, RNA was processed through the Illumina stranded mRNA prep (Illumina, 20040532) according to the manufacturer's instructions. Paired-end RNA sequencing (2 × 100 bp) was performed on an Illumina NovaSeq6000 sequencer. The RNA-seq analysis was performed using the Galaxy web server (use.galaxy.org). Raw reads were trimmed using Trimmomatic.[132] FastQC (Babraham Bioinformatics) was used before and after trimming to assess quality control. Reads were aligned to the murine reference genome (mm10) using the STAR aligner tool.[125] MultiQC (v1.12) was used to assess the quality of alignment. All aligned samples showed more than 89% uniquely mapped reads. Subsequently, reads were counted using the FeatureCounts package.[133] For DEG detection, the R package DESeq2 was used,[134] and the significant genes were defined as genes with a false discovery rate (FDR) < 0.05, with Benjimini-Hochberg multiple comparison correction and abs(logFC) > 0.5.

ATAC-seq library preparation and analysis of differential open chromatin

For ATAC-sequencing, approximately 100, 000 cells were used, and library preparation was performed according to the manual from supplier (Active Motif 53150). Reads from NGS were downsampled to an equivalent number of reads per sample using seqtk sample (version 1.2). Adaptors were trimmed with trimmomatic (version 0.39)[132] with the options ILLUMINACLIP:Trimmomatic-0.39/adapters/NexteraPE-PE.fa:2:30:10 LEADING:3 TRAILING:3 SLIDINGWINDOW:4:25 MINLEN:24. Reads were then aligned to the mouse genome (mm10) with bowtie2 (version 2.4.4)[135] using default parameters. Duplicates were removed with picard through gatk MarkDuplicates (version 4.2.5.0). Peak detection was performed using macs2 callpeak (version 2.2.7.1)[136] with the parameters ''-g mm –qvalue 0.05 –shift 100 –extsize 200 –format BAMPE –keep-dup = all –cutoff-analysis –bdg''.

QUANTIFICATION AND STATISTICAL ANALYSIS

Based on previously published works using stab-wound injury and LPS models,[10,36,39,41,54,57] we utilized similar sample sizes for all experiments performed. All statistical analyses were performed using Prism (GraphPad Software). As specified in the legends for each figure, datasets were analyzed for significance using Welch's two-tailed t test or ANOVA measures with multiple comparisons posthoc test, using $*p < 0.05$, $**p < 0.01$, $***p < 0.001$, $****p < 0.0001$; all data are presented as mean ± s.e.m.